STUDIA UNIVERSITATIS
BABEŞ-BOLYAI

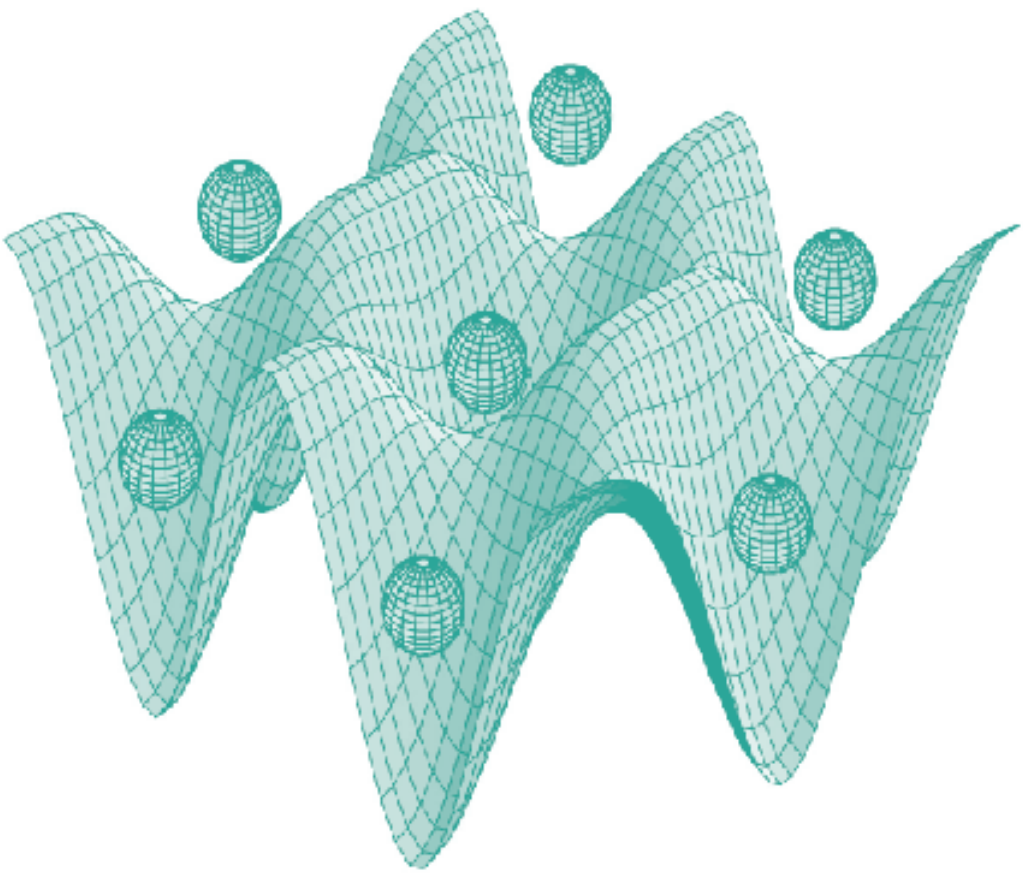

PHYSICA

2/2013

STUDIA
UNIVERSITATIS BABEŞ-BOLYAI
PHYSICA

2/2013
December

EDITORIAL OFFICE OF STUDIA UBB PYSICA:
1, M. Kogălniceanu St., Cluj-Napoca, ROMANIA, Phone: +40 264 405300
http://www.studia.ubbcluj.ro/serii/physica/index_en.html

YEAR **Volume 58 (LVIII) 2013**
MONTH **DECEMBER**
ISSUE **2**

S T U D I A

UNIVERSITATIS BABEŞ-BOLYAI

PHYSICA

2

STUDIA UBB EDITORIAL OFFICE: B.P. Hasdeu no. 51, 400371 Cluj-Napoca, Romania,
Phone + 40 264 405352

CUPRINS – CONTENT – SOMMAIRE – INHALT

ALEXANDRU OKOS, AUREL POP, CÉLINE DARIE, PIERRE BORDET, The Influence of Partial Substitution of V With Fe on Structure, Phase Purity and Microstructure of the Multiferroic $Pb(V_{1-X}Fe_X)O_3$ Compound 5

D. MARCONI, C. LUNG, MARIA TOMA, A. V. POP, The Influence of Processing Parameters on Structure of Al-ZnO Thin Films 15

M. TODICA, T. STEFAN, L. DARABAN, C. LEORDEAN, C. V. POP, Effects of Gamma Radiation on Microstructure and Electric Properties of PAA-Graphite Membranes 21

ADRIANA DEHELEAN, DANA ALINA MAGDAS, Compositional Investigations on Some Fruits Commercialized on Romanian Market 31

MIHAIL CHIRA, HORATIU VERMEŞAN, VASILE RUS, ERNEST GRUNWALD, The Corrosion Behaviour of Zn Layers, Electrodeposited on Different Substrates, by Impulse Electroplating and by Electrodeposition under Magnetic Field Methods 37

M. POP, D. FRUNZA, C. PAVEL, An Experimental and Finite Element Analysis of Material Flow During Forward Extrusion of Lead Alloy 53

E. VANEA, C. MORARU, S. MUREŞAN, R. MOLDOVAN, A. FILIP, A. MUREŞAN, S. SIMON, High Field MRI Investigation of Eye Structures after UV-B Irradiation 67

B. OPREA, C. MIRESTEAN, G. DINDELEGAN, S. SIMON, XPS and XRD Investigation of Iron Doped Nanocrystalline Hydroxyapatite 75

G. MOCANU, D. POP, Some Aspects on Pulsatory Current Electrodeposition 83

STUDIA UBB PHYSICA, Vol. 58 (LVIII), 2, 2013, pp. 5-14
(RECOMMENDED CITATION)

THE INFLUENCE OF PARTIAL SUBSTITUTION OF V WITH Fe ON STRUCTURE, PHASE PURITY AND MICROSTRUCTURE OF THE MULTIFERROIC $Pb(V_{1-X}Fe_X)O_3$ COMPOUND

ALEXANDRU OKOS[a,b], AUREL POP[a,*], CELINE DARIE[b], PIERRE BORDET[b]

ABSTRACT. The perovskite oxide $Pb(V_{1-x}Fe_x)O_3$ ($0 \le x \le 0.75$) was synthesised by solid state reaction under high pressure – high temperature conditions. The effect of the iron content on the cell parameters and phase composition were analysed by XRD, X-ray absorption spectroscopy (XAS) and EDX. The main phase is tetragonal for $x < 0.5$. At $x = 0.5$ a cubic phase appears and a mixture of the tetragonal (T) and cubic (C) phases is observed. For $x > 0.5$ the main phase is cubic. The microstructure is analysed by using SEM measurements.

Keywords: *$PbVO_3$, high pressure - high temperature synthesis, XRD, XAS, SEM, EDX.*

INTRODUCTION

Several ABO_3 perovskite compounds where A is a divalent or trivalent cation and B is the cation of a transition element are potentially multiferroic oxides [1-3]. Among these compounds $PbVO_3$ is particularly interesting. It crystallises in a tetragonal structure with the space group P4mm [4-6] which ensures the onset of ferroelectricity (similarly to $PbTiO_3$) and the V cations carry a spin 1/2 therefore the onset of some type of magnetism can be expected [7]. However, only a small magnetic signal could be detected [8, 9]. One possible explanation for the absence of a strong magnetic signal is that the d1 electrons of the V^{4+} cations are engaged in the formation of the strong vanadyl bonds which leads to a reduction of the magnetic moment and to the formation of a 2D AFM system [9]. Bulk $PbVO_3$ samples can only be synthesized under high pressures [5]. We observed that the synthesis pressure can be lowered at the expense of the sample quality. These results have been published

[a] *Babes-Bolyai University, Faculty of Physics, Str. Kogălniceanu, Nr. 1, RO-400084 Cluj-Napoca, Romania,*
* *Corresponding author: aurel.pop@phys.ubbcluj.ro*
[b] *Néel Institute, CNRS/UJF, UPR2940, 25 Rue des Martyrs, BP 166, 38042, Grenoble Cedex 9*

elsewhere [10]. Our samples with majority of phase $PbVO_3$ were obtained by solid state reaction method, using a new set of milder reaction conditions at a pressure of 4 GPa and temperature in the range of 650°C to 1000°C. XRD shows that along with the majority $PbVO_3$ phase some minority phases are present. By increasing HT from 650°C to 1000°C, the intensity of the Bragg peaks for the minority phases decreases, and the impurity phases were diminished [10]. The substitution of vanadium by iron could reduce the 2D character and allow the onset of a 3D magnetic ordering. The synthesis of the $PbV_{1/2}Fe_{1/2}O_3$ compound was first reported by Tsuchiya [12]. The reaction conditions employed by Tsuchiya were a pressure of 7 GPa and temperature in the range of 800-1000° C. The substitution maintained the tetragonal unit cell. The magnetic moments of the iron cations from the above system were shown to be antiferromagnetically coupled. We obtained by using the solid state reaction method the $PbV_{1-x}Fe_xO_3$ compounds with $x \leq 0.3$. The amounts and types of impurity phases were found to be strongly dependent on the composition and the preparation conditions. The highest content of tetragonal P4mm phase having the starting composition x=0.3 was obtained when the sample was sintered at T = 1100°C and p = 6 GPa [11]. In this note we report the evolution of the cell parameters of the $Pb(V_{1-x}Fe_x)O_3$ system for $0 \leq x \leq 0.75$ and we report the formation of a new phase with cubic symmetry for $x \geq 0.5$.

EXPERIMENTAL

Polycrystalline $Pb(V_{1-x}Fe_x)O_3$ samples were synthetised by solid state reaction under conditions of high pressure and high temperature on a CONAC type apparatus. The pressure was set at 6 GPa and the temperature was set at 950° C. The reaction time was 90 minutes. Stoichiometric quantities of high purity (99.99 %) PbO, PbO_2, V_2O_3, V_2O_5 and Fe_2O_3 were used as starting products. For $x < 0.5$, the chemical reaction that produces the compound is described by the following equation:

$$4\ PbO + (1-2x)V_2O_3 + V_2O_5 + 2x\ Fe_2O_3 \rightarrow 4\ PbV_{1-x}Fe_xO_3.$$

Samples with x = 0.0, 0.1, 0.2, 0.3 and 0.4 were obtained.

When x = 0.5 the coefficient of V_2O_3 vanishes (1-2x=0) as V_2O_3 is no longer needed for the synthesis.

For samples with x = 0.6 and 0.75 Fe, in order to maintain the oxygen stoichiometry, PbO_2 needs to be added. The equation of the chemical reaction therefore becomes:

$$(3+x)\ PbO + (1-x)\ PbO_2 + 2(1-x)V_2O_5 + 2x\ Fe_2O_3 \rightarrow 4\ PbV_{1-x}Fe_xO_3.$$

XRD was used for the characterization of the phase type, phase purity and variation of the cell parameters. The XRD patterns were collected on a Siemens D5000 diffractometer working in transmission geometry, using the Cu Kα1 radiation, a step

size of 0.016 and 10 s counting time / step. The diffractograms were refined using the Rietveld method with the Fullprof software. The microstructure of the samples was investigated by using a Zeiss SEM. The chemical composition was verified by EDX spectrometry. The acceleration voltage was set at 20 kV and the working distance was set at 8 mm. XAS measurements were conduced on the vanadsium absorption edge at the BM 32 FAME French CRG beamline of the ESRF synchrotron facility, Grenoble.

RESULTS AND DISCUSSION

Figure 1 shows the XRD patterns for the samples with $0.0 \leq x \leq 0.6$ Fe. XRD patterns for the samples with $0.0 \leq x \leq 0.4$ evidenced that these samples contain essentially a single phase with the $PbVO_3$ structure, with the same diffraction peaks and Miller indices (hkl) as in reference [5]. This result is confirmed by EDX measurements. For example, figure 2 shows the Rietveld refinement for the x=0.3 Fe sample. The calculated XRD pattern is shown in a continuous line. The ticks under the diagrams mark the position of the Bragg peaks. The bottom line which gives the difference between the observed and calculated patterns shows the good agreement between the experimental data and the calculated spectra.

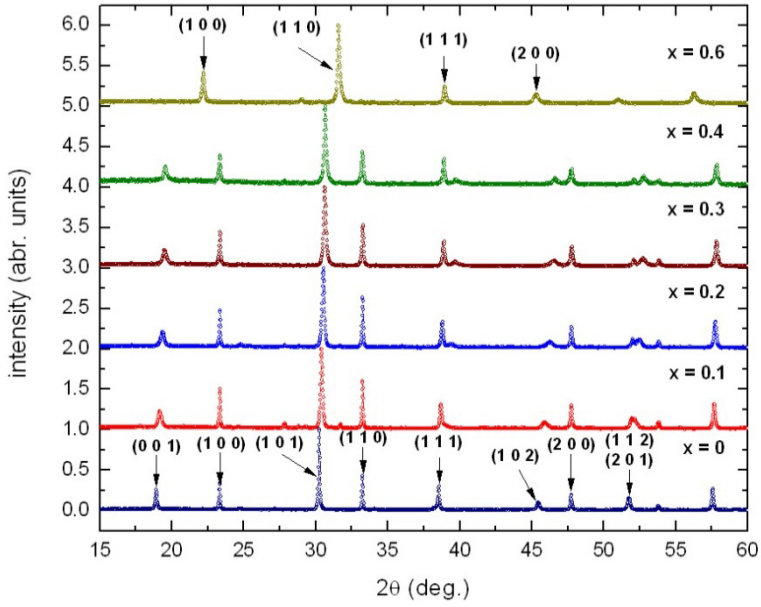

Fig. 1. XRD data for the samples with $0.0 \leq x \leq 0.6$ Fe.

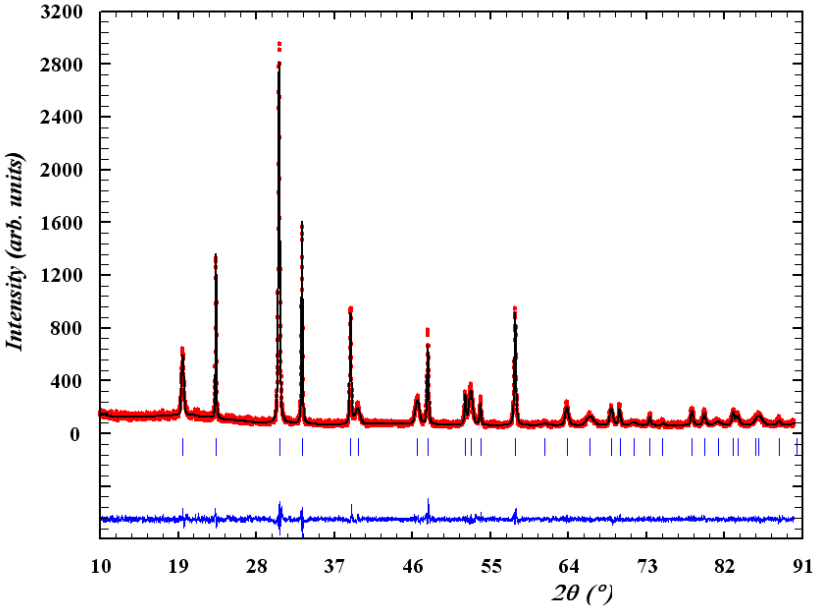

Fig. 2. Rietveld refinement for sample with x=0.3 Fe. The red dots mark the experimental data. The black line shows the calculated diffraction pattern and the bottom line which gives the difference between the observed and calculated patterns.

Figure 3 show the dependence of the tetragonal lattice parameters (a=b, c) function of Fe content x (in at%). The lattice parameter a=b does not change with the composition. For samples with $x \leq 0.5$, the unit cell height c (lattice parameter c) linearly decreases with increasing x. The lattice parameters for $PbVO_3$ (x=0.0 sample) are a = 3.80 Å and c = 4.67 Å.

By increasing the Fe content to x=0.5 sample the parameter remain unchanged (a = 3.80 Å) but the unit cell height decreases to c = 4.49 Å. In this sample (x = 0.5), XRD shows a mixture of the tetragonal (T) and cubic (C) phases. The majority phase (more than 95%) is the tetragonal phase. The lattice parameter for the new cubic phase is close to 4 Å.

For x > 0.5 the cubic phase becomes the main phase (see fig.1 for sample with x=0.6Fe). The space group of the cubic phase is Pm3m and the lattice constant is close to 4 Å. The value of the lattice constant of the cubic phase does not change considerably with the x content. A possible explanation is that the nominal composition can differ from the actual chemical composition of the samples with the cubic symmetry. XRD shows the presence of several impurities which supports the idea of the difference between the nominal and actual composition.

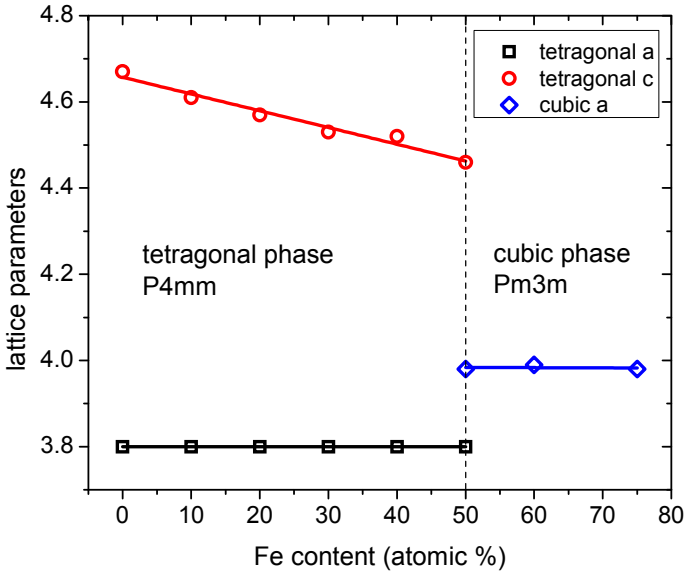

Fig. 3. The dependence of the unit cell parameters function of Fe content. Dots represent the experimentally determined values. Continuous lines are linear fits of the experimental data. The dotted line marks the transition form the tetragonal phase to the cubic phase.

Figure 4 shows the Rietveld refinement for the x=0.6 sample. The first row of ticks marks the Bragg peaks of the main cubic phase. The second row of ticks marks the diffraction peaks of $Pb_3V_2O_8$, indexed according to [13, 14]. The third row marks the diffraction peaks of a secondary cubic phase which is probably constituted by platinum dust that leached from the reaction capsule. A few more unidentified peaks are visible in the range of 2θ between 30 and 40°. These peaks are probably generated by starting products that have not reacted.

Figure 5 shows the XAS data for the vanadium K edge. The position of the pre-peak reveals the presence of V^{4+} and V^{5+}. The pre-peak is shifted towards the right as the iron content increases. This indicates the increase of the number of V^{5+} cations with the increase of x. The peak obtained for $PbVO_3$ shows the presence of only V^{4+} cations. The peak of the x = 0.5 sample shows the presence of only V^{5+} cations. The reason for this shift is the fact that the substitution of vanadium with iron (V-Fe) is not isovalent if V^{4+} is substituted by Fe^{3+}. When the substitution takes place, some V^{4+} cations from the sample change their oxidation state to V^{5+} in order to restore the charge balance and maintain an average oxidation of 4+ at the B site.

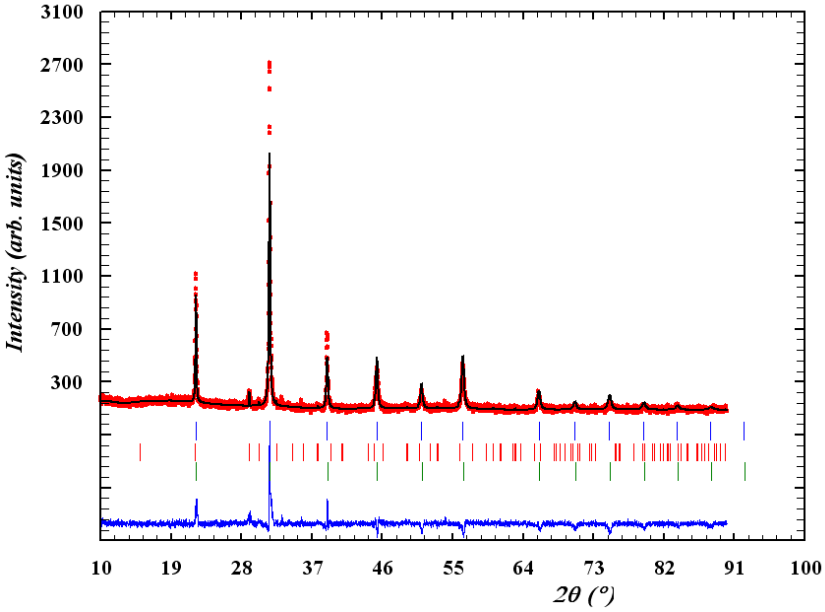

Fig. 4. Rietveld refinement for the sample with x = 0.6 Fe.

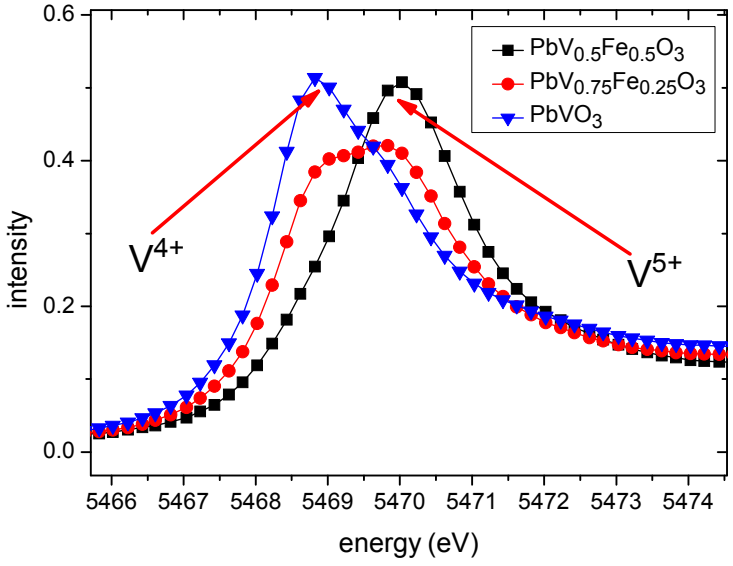

Fig. 5. XAS data for the V k edge for the following samples:$PbVO_3$, $PbV_{0.75}Fe_{0.25}O_3$ and $PbV_{0.5}Fe_{0.5}O_3$.

The number of vanadium cations that undergo this transition is (must be) equal to the number of iron cations substituted in the sample. The replacement of the V^{4+} cations is therefore two fold. On one hand the V^{4+} cations are directly replaced by the iron cations and on the other hand some of the remaining V^{4+} cations undergo the transition to V^{5+}. The composition of the samples can therefore be written as $Pb(V^{4+}_{1-2x}V^{5+}_{x}Fe^{3+}_{x})O_3$. It can be observed that for x = 0.5 all the V^{4+} cations are exhausted and consequently the sample contains only V^{5+} and Fe^{3+} cations (result consistent with the need / choice of starting oxides). This can also explain why the solid solution stops at x = 0.5.

Figure 6 shows EDX spectrum for x=0.3 sample. The composition of the sample determined by EDX is $Pb_{0.99}V_{0.71}Fe_{0.28}O_3$ which is close to the nominal composition of $PbV_{0.7}Fe_{0.3}O_3$. However, the oxygen content was not determined. The samples are well crystallised. This can be observed by SEM from the cubic shape of the crystallites. The SEM image also reveals the presence of ferroelectric domains which are recognised as stripes of alternating contrast (see figure 7). This feature was observed for all the samples with tetragonal symmetry.

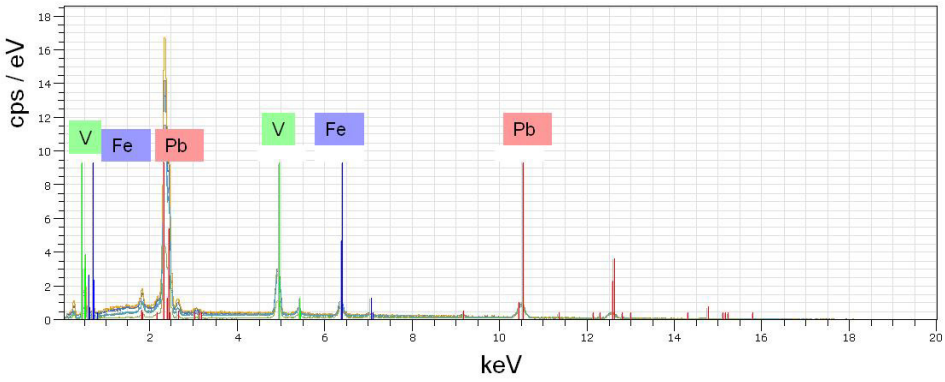

Fig. 6. EDX spectrum of the sample with x=0.3 Fe.

The EDX spectra for the sample x=0.6 with cubic structure are shown in figure 8. The composition determined by EDX for this sample is $Pb_{1.03}V_{0.46}Fe_{0.51}O_3$. This composition is slightly different form the nominal composition of $PbV_{0.4}Fe_{0.6}O_3$ (x=0.6 Fe) and suggests the formation of a compound with x closer to 0.5 rather than 0.6 (the nominal stoichiometry). This result is consistent with the absence of any significant variation of lattice parameters of the cubic phase with the iron content despite the wide range of compositions (see figure 3).

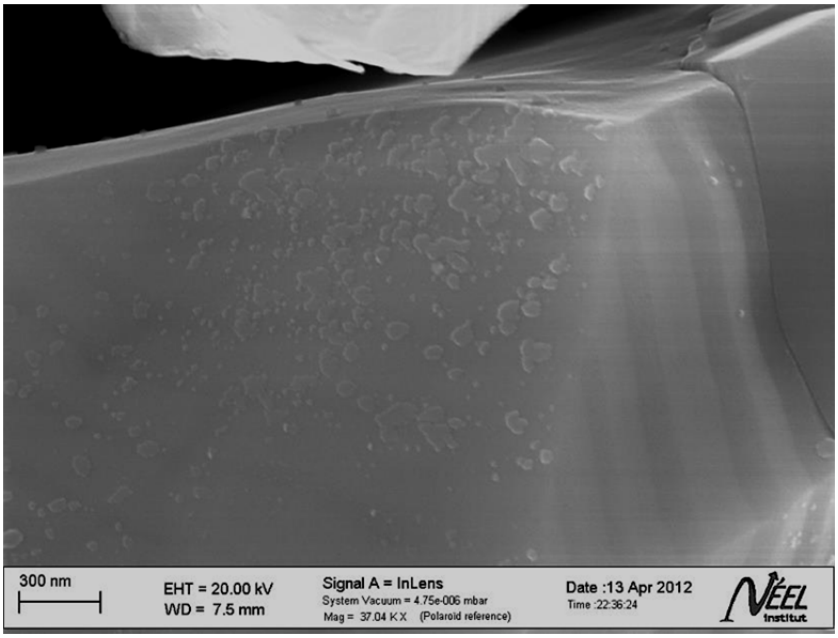

Fig. 7. Crystallite from the sample with x= 0.3Fe revealing the presence of ferroelectric domains (the vertical stripes on the right part of the figure).

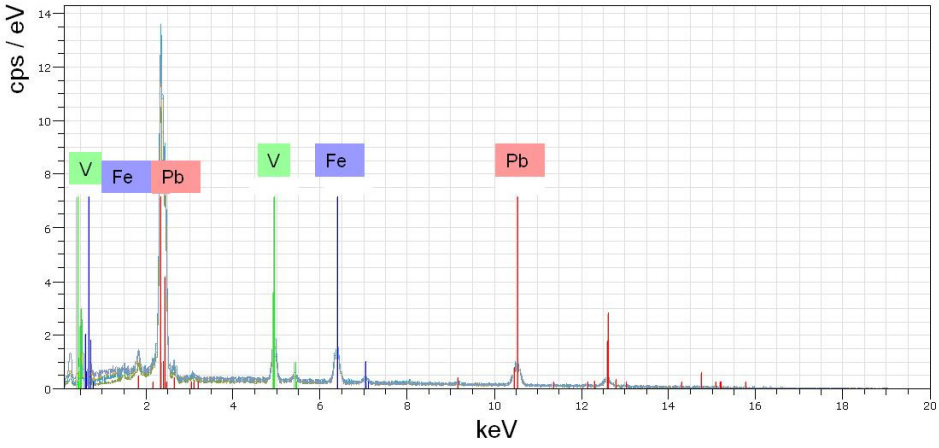

Fig. 8. EDX spectra for the sample with x = 0.6 Fe.

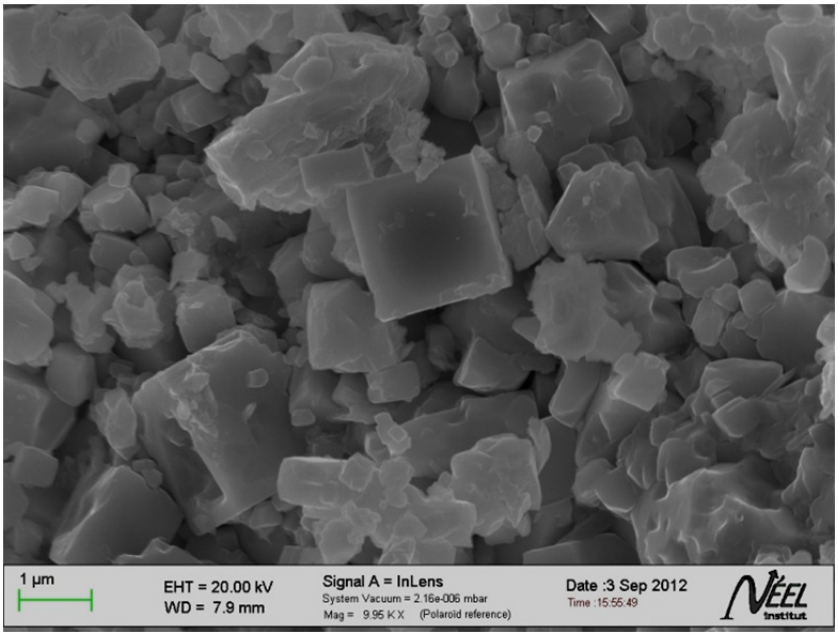

Fig. 9. SEM image of crystallites from sample with x=0.6 Fe.

Figure 9 shows a SEM image of crystallites from the sample with x=0.6 Fe. The sample is well crystallized and the presence of cubic shaped crystallites supports this observation. EDX measurements show that some of the cubic shaped crystallites are of the starting oxide Fe_2O_3 which did not took part to the reaction. The presence of Fe_2O_3 (seen by EDX) and secondary phases (seen by XRD) can explain the difference between the experimentally determined composition and the nominal one.

CONCLUSIONS

By using the solid state reaction method under extreme conditions (pressure of 6 GPa and temperature of 950°C) the $PbV_{1-x}Fe_xO_3$ ($0 < x < 0.75$) compounds were obtained.

For samples with $x < 0.5$ Fe the main phase corresponds to the tetragonal structure in the space group P4mm. The a = b lattice constants do not depend on Fe content and the unit cell height c decreased linearly with increasing iron content.

The compositions of the samples with $x < 0.5$ were little different from those expected from starting compositions.

XRD for samples $x \geq 0.5$ shows a cubic phase. The value of the lattice constant of the cubic phase does not change considerably with Fe content. The difference between the nominal and actual composition above x = 0.5 is related to the occurrence of several impurities.

XAS measurements revealed that the samples contain a mixture of V^{4+} and V^{5+} cations and that the number of V^{5+} cations increases with increasing x. For x = 0.5 all the V^{4+} cations are exhausted and the sample contains only V^{5+} and Fe^{3+} cations.

ACKNOWLEDGEMENTS

This work was possible with the financial support of the Sectoral Operational Programme for Human Resources Development 2007-2013, co-financed by the European Social Fund, under the project number POSDRU/107/1.5/S/76841 with the title „Modern Doctoral Studies: Internationalization and Interdisciplinarity".

REFERENCES

[1]. N. Hill, *J. Phys. Chem. B*, *104,* 6694-6709 (2000).
[2]. J. Kreisel, W. Kleemann, R. Haumont, *Reflets de la Physique*, 8, 10 (2008).
[3]. N. Hur, S. Park, *Nature,* 429 (2004).
[4]. Alexei A. Belik, M. Azuma, Takashi Saito, *Chem. Mater.* 17, 269-273 (2005).
[5]. Roman V. Shpanchenko, V.V. Chernaya, A. A. Tsirlin, *Chem. Mater.* 16, 3267-3273 (2004).
[6]. Lane W. Martin, M. Chi, Teruyasu Mizoguchi, Jens Kreisel, *Applied Physics Letters*, 90, 062903 (2007).
[7]. D.J. Singh, *Physical Review B 73*, 094102 (2006).
[8]. A. Tsirlin, A. Belik, R. Shpanchenko, *Physical Review B*, 77, 092402 (2008).
[9]. Kengo Oka, Ikuya Yamada, Masaki Azuma, Mikio Takano, *Inorganic Chemistry*, 47, 7355 (2008).
[10]. Alexandru Okos, Aurel Pop, Céline Darie, Pierre Bordet, *Studia Chemia*, LVIII, 57-62 (2013).
[11]. Alexandru Okos, Aurel Pop, Céline Darie, Pierre Bordet, OAM-in press 2013.
[12]. Takeshi Tsuchiya, Tetsuhiro Katsumata, Journal of the Ceramic Society of Japan, 117, 102-105 (2009).
[13]. J.M. Kiat, P. Garnier, M. Pinot, *Journal of Solid State Chemistry*, 91, 339 (1991).
[14]. J.M. Kiat, P. Garnier, G. Calvarin, M. Pinot, *Journal of Solid State Chemistry*, 103, 490 (1993).

STUDIA UBB PHYSICA, Vol. 58 (LVIII), 2, 2013, pp. 15-20
(RECOMMENDED CITATION)

THE INFLUENCE OF PROCESSING PARAMETERS ON STRUCTURE OF Al-ZnO THIN FILMS

D. MARCONI[a,b,*], C. LUNG[a], MARIA TOMA[a], A. V. POP[a]

ABSTRACT. ZnO and 1.5%Al-doped ZnO (Al:ZnO) thin films were deposited on glass substrate using RF magnetron sputtering technique. The influence of substrate-target distance and the partial pressure of oxygen in sputtering gas on the structure of thin films is analyzed by X-Ray diffraction (XRD). From (XRD), it is found that all films are highly oriented with their crystallographic *c*-axis perpendicular to the substrate and that the grain size is influenced by both target-substrate distance and oxygen concentration in flow sputtering gas.

Keywords: Al-*ZnO thin films, RF magnetron sputtering, XRD.*

INTRODUCTION

Zinc oxide (ZnO) is one the most important II-VI semiconductor, known for its many potential applications such as thin films for optoelectronic, window materials in solar cells, laser diodes, transparent conductive contacts, and piezoelelectric applications and many others [1,2]. Compared with undoped ZnO, the Al-doped ZnO (AZO) films have a lower resistivity and better stability [3].

Several techniques have been used to fabricate epitaxial and textured ZnO and AZO films including magnetron sputtering and pulsed-laser deposition (PLD) [4-7]. Magnetron sputtering technique is considered one of the best techniques in deposition of thin films, as it allows growth of uniform thin films at low temperature with high reproducibility, with strong adhesion to substrates over large area surfaces [8]. Many reports already showed that the properties of AZO

[a] *Babes-Bolyai University, Faculty of Physics, M. Kogalniceanu No. 1, 400084, Cluj-Napoca, Romania*
[b] *Department of Molecular and Biomolecular Physics, National Institute for Research and Development of Isotopic and Molecular Technologies, Donath 63-105, 400293 Cluj-Napoca, Romania*
* *Corresponding author: daniel.marconi@phys.ubbcluj.ro*

thin films were mainly influenced by processing parameters during sputtering, such as substrate temperature, discharge power, target-substrate distance and oxygen flow content [4,5,9-11,13,15].

In this paper we report on the growth and characterization of epitaxial AZO films on glass substrates, by using different substrate-target distance and different oxygen concentration in the flow sputtering gas, respectively. The structural properties of the AZO films grown by R.F. magnetron sputtering were also characterized.

Experimental

The ZnO and Al doped ZnO thin films were deposited by RF magnetron sputtering technique. Ceramic circular targets with chemical compositions ZnO and $Al_{0.015}Zn_{0.985}O_x$ (sample AZO) were obtained by solid state reaction method, using mechanical mixed powders of 99.99% pure ZnO and 99.97% pure Al_2O_3. The films were deposited on glass substrate by using the oxygen–argon atmosphere as sputtering gas. The substrate temperature was 150 ^{0}C. The reactive gas is formed from Ar and O_2 mixtures, having the mass flows d_{Ar} and d_{O2}. The introduction of the reactive gas to the sputtering chamber was independently analyzed using two mass flow controllers. The deposition pressure in the chamber was 2×10^{-2} mbar. The crystallinity of AZO films was investigated with respect to the distance d between target and substrate and fraction of oxygen in sputtering gas, respectively. By using the same fraction of oxygen in sputtering gas f_{O2} = 0.375, three films corresponding to the target-to-substrate distance d = 4; 6 and 8 cm were obtained. For the distance target-substrate d = 6 cm, four films were obtained, by using the values f_{O2} = 0; 0.375; 0.50 and 0.75 for the fraction of oxygen in sputtering gas.

The film structure and the preferred orientation of crystallites were determined by X-ray diffraction (XRD) analysis, using a Brucker X-ray diffractometer with a Cr K_α radiation. The 2θ range of 45 – 60º was recorded at the rate of 0.02º and 2θ / 0.5 s. The crystal phases were identified comparing the 2θ values and intensities of reflections on X-ray diffractograms with JCP data base using a Diffraction AT-Brucker program.

RESULTS AND DISCUSSION

Figure 1 shows the XRD diffraction patterns of Al-ZnO thin films obtained by using in sputtering synthesis different distances d between target and substrate. As shown in Fig. 1, the diffraction pattern shows only the maximum

with Miller indices (002). This peak detected at about 51.5° is attributed to the wurtzite structure of the growing films with the c-axis oriented perpendicular to the substrate surface. For the film AZO4 (d = 4 cm) the (002) peak of AZO is symmetric. The (002) peak of AZO6 (d = 6 cm) film become asymmetric and is shifted to left. This shift is associated with the decrease of the height of unit cell, c.

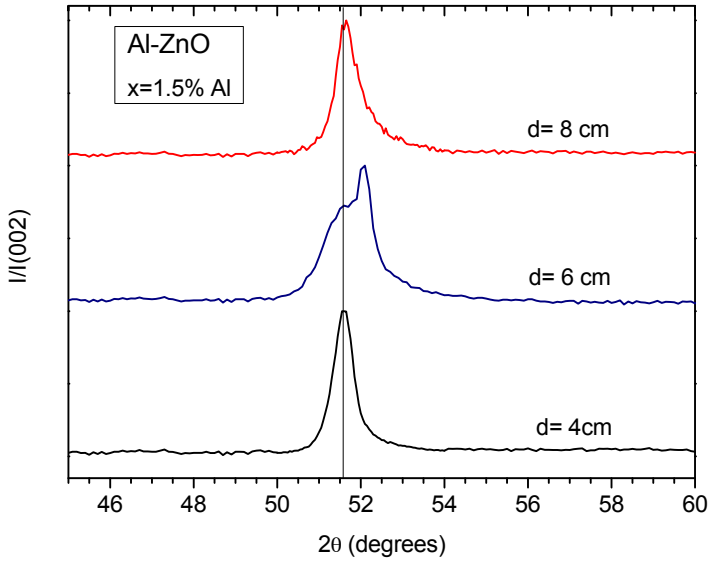

Figure 1. The XRD spectra of Al-ZnO (x=1.5% Al) films grown at the same fraction of oxygen (f_{O2} = 0.375) in sputtering gas and varying distance d between target and substrate.

The lattice constant c of the samples calculated by Bragg formula (Table 1) evidenced a small decrease from c = 0.585 nm for d = 4 cm to 0.579 nm for d = 6 cm.

Table 1.

Al-ZnO films x=1%Al;f_{O2} =0.375	d [cm]	D [nm]	c [nm]
AZO 4	4	26	0.585
AZO 6	6	13	0.579
AZO 8	8	24	0.585

The vertical line shows that the shoulder of the (002) peak of AZO6 film is in the same position as the peak of AZO4 film. This result suggest that in AZO6 film, the growing of crystal on the direction normal to substrate lead to two different values of height of unit cell (centered around the values 0.585 nm and

0.579 nm).The changes in (002) peak of AZO6 film suggest that a moderate quantity of Al atoms can exist at interstitial sites and confirmed the structural modification of ZnO matrix. The crystallite sizes of the films were calculated using the Scherrer equation [5,12,13,15]. The mean grain size decreases from 26 nm to 13 nm when d is increased from 4cm to 6 cm (Table 1). For AZO8 film the (002) peak is in the same position that in AZO4 film, the same value of unit cell height c and a little different value of crystallite size D (Table 1). The best cristallinity with D= 26 nm was obtained for d = 4 cm (film AZO4).

X-ray diffraction patterns of the films prepared at different values of f_{O2} are shown in Fig. 2.

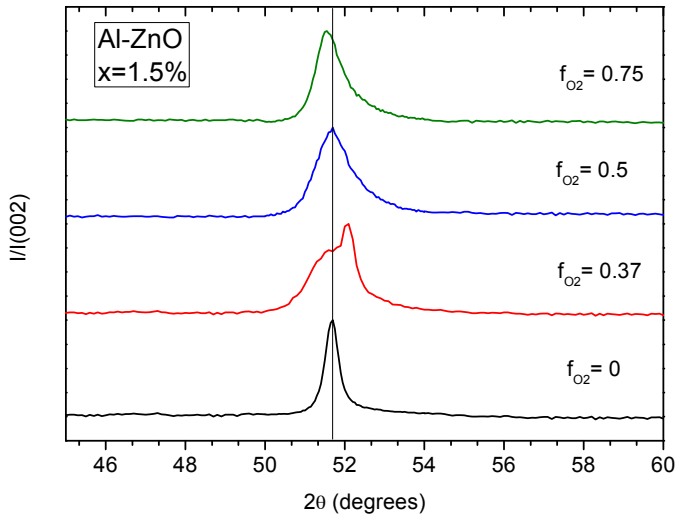

Figure 2. The XRD spectra of Al-ZnO (x=1.5% Al) films grown at the same distance target substrate d=6 cm and varying the value f_{O2} of oxygen in sputtering gas.

XRD for these thin films indicates the epitaxial growth in the direction of c by increasing f_{O2}. It appears that for f_{O2} = 0 (film AZOf0) the peak (002) is symmetric and narrow. By increasing f_{O2} to 0.375 (film AZOf2), the peak splits partially into two components: the unresolved maximum found the same value 2θ as the peak for the film obtained at f_{O2} = 0 and a narrow maximum shifted to the right. For f_{O2} = 0.5 and 0.75 we have a broad and asymmetric single peak. This asymmetry is due to the contribution of the narrow peak highlighted for f_{O2} = 0.375, which may be associated with a structure having a height of unit cell c different from c value of the film with f_{O2} = 0.

Table 2 shows that the height of unit cell c little change by increasing the oxygen content with value, except for the film obtained for f_{O2} = 0.375 (decreases the value of the unit cell height c = 0.580 nm).

Table 2.

Al-ZnO films x=1%Al;d=6 cm	f_{O2}	D [nm]	c [nm]
AZO f0	0	34	0.584
AZO f1	0.375	12	0.580
AZO f2	0.5	14	0.584
AZO f3	0.75	18	0.582

The highest value of average crystallite size D = 34 nm and the best crystallinity is obtained for f_{O2} = 0. The increase of f_{O2} lead to a decrease in the average grain size, so these films are lower cristalinity that those obtained in the absence of oxygen in sputtering gas. The excess of oxygen might induce defects in the films, which influenced the nucleation and growth of the films, and finally the degradation of the crystallinity in agreement with other results [4,11, 14].

CONCLUSIONS

Epitaxial ZnO thin films doped with 1.5%Al deposited on glass substrates were obtained by radio-frequency (RF) reactive magnetron sputtering method. XRD facts that the main effect of increasing the distance target-substrate in the synthesis of ZnO thin films is the change in the mean value of the grain size. The best crystallite size is obtained for d = 4 cm. As the oxygen content in gas flow was increased, the linewidth of (002) diffraction peak was increased and a poorer crystallinity was shown. The highest value of average crystallite size D = 34 nm, and the best crystallinity is obtained for f_{O2} = 0 and a distance target-substrate d = 6 cm.

REFERENCES

[1] V.S. Khomchenko, T.G. Kryshtab, A.K. Savin, L.V. Zavyalova, N.N. Roshchina, V.E. Rodionov, O.S. Lytvyn, V.I. Kushnirenko, V.B. Khachatryan, J.A. Andraca-Adame, *Superlattice Microstructures,* **42** (2007), 94-98.

[2] M. Zeman, Poortmans, J. & Arkhipov, V., John Wiley & Sons, 978-0-470-09126-5, New York (2007), 173.

[3] V.N. Zhitomirsky, E. Cetinorgu, E. Adler, Yu. Rosenberg, R.L. Boxman, S. Goldsmith, *Thin Solid Films,* **515** (2006), 885.
[4] Dorina Gîrbovan, D. Marconi, R. Redac, A.V. Pop, *Optoelectronics and advanced materials,* **6** (9-10), (2012), 859 – 862.
[5] Dorina Gîrbovan, M.A. Bodea, D. Marconi, J.D. Pedarning, A.V. Pop, *Studia Universitatis Babeş-Bolyai Chemia,* 56 (**3**), (2011), 213-220.
[6] D. Ciomos, D. Marconi, R. Redac, A. V. Pop, *Studia Universitatis Babeş-Bolyai Physica,* LVI (**1**), (2011), pg. 3-8.
[7] J.D. Pedarnig, J. Heitz, T. Stehrer, B. Praher, R. Viskup, K. Siraj, A. Moser, A. Vlad, M.A. Bodea, D. Bauerle, N. Hari Babu, D.A. Cardwell, *Spectrochim. Acta* B, **63,** (2008), 1117.
[8] J. Lee, D. Lee, D. Lim, K. Yang, *Thin Solid Films,* **515** (2007), 6094.
[9] M. Chen, Z.L. Pei, C. Sun, J. Gong, R.F. Huang, L.S. Wen, J. *Mater. Sci. Eng. B*., **85** (2001), 212.
[10] S. Kobayakawa, Y. Tanaka, A. Ide-Ektessabi, *Nucl. Instr. Meth. Phys. Res. B*., **249** (2006), 536.
[11] Dong-Hyun Hwang, Jung-Hoon Ahn, Kwan-Nam Hui, Kwan-San Hui, Young-Guk Son, *J. Ceram. Proc. Res*., **12** (2011), 150.
[12] J.J. Ding, S.Y. Ma, H.X. Chen, X.F. Shi, T.T. Zhou, L.M. Mao, *Physica B,* **404** (2009), 2439.
[13] Y.H. Kim, K.S. Lee, T.S. Lee, B. Cheong, T.-Y. Seong, W.M. Kim, *Appl. Surf. Sci*., **255** (2009), 7251.
[14] Y.R. Sui, B. Yao, L. Xiao, L.L. Yang, J. Cao, X.F. Li, G.Z. Xing, J.H. Lang, X.Y. Li, S.Q. Lv, X.W. Meng, X.Y. Liu, J.H. Yang, *Appl. Surf. Sci*., **287** (2013), 484–489.
[15] Chandan Ashis Gupta, Sutanu Mangal, Udai P. Singh, *Appl. Surf. Sci*., **288** (2014), 411–415.

STUDIA UBB PHYSICA, Vol. 58 (LVIII), 2, 2013, pp. 21-29
(RECOMMENDED CITATION)

EFFECTS OF GAMMA RADIATION ON MICROSTRUCTURE AND ELECTRIC PROPERTIES OF PAA-GRAPHITE MEMBRANES

M. TODICA[a,*], T. STEFAN[a], L. DARABAN[a], C. LEORDEAN[a] AND C. V. POP[a]

ABSTRACT. Electric conducting polymeric membranes based on poly acrylic acid (PAA) were obtained by addition of graphite to the polymeric matrix. The possibility to modify the electric properties by gamma irradiation was tested. The possible interactions between the polymer and the graphite and the effects of gamma radiation on the structure of the system were studied by Raman spectroscopy.

Keywords: *Poly acrylic acid membranes electric conductivity, graphite*

INTRODUCTION

In the last time the fabrication of medical pharmaceuticals with controlled release of the active substance is one on the greatest challenge of the pharmaceutical industry. The advantage of such pharmaceutical are the possibility to apply the active substance only in the desired area of the tissues, the release of the drug with a controlled rate, the reduction of the quantity of the active substance and the diminution of the migration of the drug in the health zones of the body, [1,2]. One of the methods to achieve this purpose is the use of polymeric matrix. Polymers are suitable for this aim because they are chemically stables in contact with the tissues, are biocompatible, and they are characterized by a structure with spaces which can includes the active substances. Moreover these materials don't react chemically with the drugs, avoiding the apparition of the undesired new chemical compounds. However an important challenge concerning these systems is the modality of release of the drug. The simplest way is the dissolution of the matrix

[a] *"Babes-Bolyai" University, Faculty of Physics, M. Kogalniceanu No 1, 400084 Cluj-Napoca, Romania,*
* *Corresponding author: M. Todica, e-mail: mihai.todica@phys.ubbcluj.ro, tel. +40264405300*

under the action of the biological liquids. In this case the delivery rate depends on the quantity of biological liquids in contact with the pharmaceutical, the concentration of these liquids and the time of theirs actions. The polymer must have a specific chemical composition which allows the destruction of the matrix by the biological fluids. These requests are generally difficult to fulfill. Other possibility is the activation of the release process by irradiation with different radiations. This way requests also the use of special matrix which can be destroyed by the radiation that represents an expensive solution. One of the simplest ways is the activation process by local heating. Heat can be obtained by electric currents passing trough the polymeric matrix. For this purpose the matrix must have a characteristic electric conductivity. The conductivity can be intrinsic or can be obtained by doping the matrix with different inorganic compounds or under intense gamma irradiation, [3, 4]. In this work we studied the possibility to obtain polymeric membranes with desired electric conductivity by doping the polymer and by irradiation. We used membranes of poly acrylic acid (PAA) as matrix and the graphite as dopant. The interest was the study of the electric properties of the system in function of the dopant concentration and the influence of gamma radiation on the electric conductivity. In addition we were interested on the observation of the possible interactions between the dopant and the polymer and the possible modifications induced by radiation on the structure of the system. Such investigations concern the neutrality of the dopant towards the polymeric matrix. For this purpose we performed electric investigations of conductivity and Raman measurements.

EXPERIMENTAL

The PAA membranes were prepared by mixing 2 hours the polymer in powder state with distilled water at room temperature until a homogeneous gel is obtained. The acid character of the gel was eliminated by neutralization with small quantities of TEA until the PH=7. The graphite was added in desired concentration, (1, 5, 15 and 30%) to the gel before neutralization. The composition was displayed on glass plates and kept in dark at room temperature 24 hours until water completely evaporates. The gamma irradiation was performed with ^{60}Co source with the dose rate of 5.6 Gy per hour until the dose of 1.5 KGy was accumulated, [5]. For the electric measurements the membranes were placed between two circular cooper golden plated electrodes with 5 cm diameter and controllable distance between them. The resistivity vas measured with high impedance Orion terra ohmmeter. The Raman investigation were performed with Witec R 3000 CN systems, with excitation power 150 mW at wavelength λ = 785 nm.

RESULTS AND DISCUSSIONS

Table 1

Sample	Resistivity [Ωm] Before irradiation	Resistivity [Ωm] after irradiation
PAA pure	$50*10^9$	$49*10^9$
PAA+1%C	5600	3450
PAA+5%C	900	750
PAA+15%C	380	270
PAA+30%C	180	130
Graphite pure	1.8	1.5

PAA is one of the polymers largely used actually in the pharmaceutical industry as carrier for the active drugs, [6]. Previous studies show that PAA matrix can include in its matrix the clotrimazole, [7]. It is a hydrophilic polymer with very good biocompatibility. The matrix is determined by the spontaneous arrangement of the long polymeric chains in disordered structures. Usually the polymeric structure is amorphous, with physical entanglements, without chemical bonds, between the chains, [8]. This structure is characterized by the existence of large empty domains, (pores or holes), which can be occupied by the medical drugs. The polymer must be chosen so that no chemical interaction appears with the drug. The drug can be eliminated from these holes by diffusion. Diffusion can be stimulated by heat. The simplest way to produce local heat, and control the heating, is the use of the electric currents. But the polymer itself, in pure state, has a very low electric conductivity. Its electric conductivity can be increased substantially by introducing small quantities of graphite in its structure, [9]. The system polymer dopant appears as a porous structure containing in its holes conductive substance. These conductive domains appear as island dispersed into an electric insulator. The electric conduction appears when these domains became in physical contact, allowing the passage of conducting electrons. It is evident that the number of such contacts depends on the concentration and distribution of the conducting domains. But the size and the distribution of these domains are affected by the length and the local fluctuations of the polymeric chains. Log chains provides a more stable structure, with low frequency fluctuations, whereas short chains allows more rapid fluctuations and easier apparitions of physical contacts between the occupied domains by the graphite. Modification of the length of the chains appears spontaneously due to the thermal agitation, but the probability of such events is low. More pronounced effect can be provoked from the outside, for example by irradiation with high energy radiations. Generally the effect of irradiation is the breaking of the polymeric chains. After irradiation the mobility of the chains increases facilitating the rearrangement of the

molecules and the apparition of new holes in the structure of the polymer. The probability of apparition of new connections between the domains occupied by the graphite increases. As result the electric conductivity of the system increases also. This behavior was observed for ours samples. The pure polymeric gel, before irradiation, is characterized by very high resistivity. This property is due to the fact that PAA don't contains free conductive electrons along the polymeric chains. After introduction of small quantity of graphite, i.e. 1%, the electric conductivity increases significantly. As presented above, the graphite occupies the free spaces exiting in the structure of the polymer, and the electric conduction occurs when these domains become in physical contact. As the concentration of graphite increases the fraction of holes occupied by the graphite increases also, and the electric conductivity increases. The evolution of the resistivity in function of the graphite concentration is shown in Table 1 and figure 1. After irradiation, for a given concentration of the graphite, the electric resistivity decreases, (Table 1, Fig.1). This behavior was explained above. We analyzed separately the conductivity of pure gel and then the conductivity of doped samples before and after irradiation.

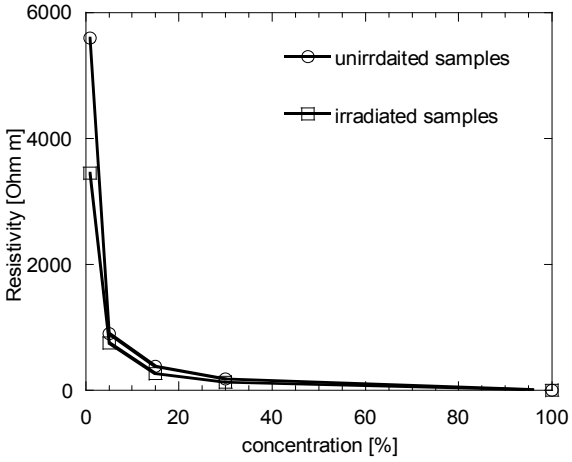

Fig. 1. The resistivity of pure PAA membranes with different concentrations of graphite before and after irradiation

We can observe a very small increase of the conductivity of the pure gel. This fact is determined by the apparition of some free electrons and ions after irradiation, consequence of the breaking chains. However the number of such ions is very low, fact that explains the low electric conductivity of the polymer after

irradiation. The contribution of the polymer is so small that it can be neglected for samples containing graphite. In the doped samples the conduction is determined almost exclusively by the graphite. As results from these investigations the irradiation at this dose doesn't affect dramatically the electric conductivity of the system PAA-graphite. The conduction is mainly determined by the graphite. Some practically conclusions result from these observation. The electric conductivity can be controlled by the concentration of the graphite, and the system PAA-graphite has a relatively high stability against the gamma radiation. Moderate irradiation doesn't destroy the structure of the polymer and doesn't affect essentially its electric conductivity.

The electric measurements give information on molecular long range scale of the system, without the possibility to observe eventually interactions between the polymer and the dopant or the effect of radiations on the local structure of the system. Such observations were done by Raman spectroscopy, [10].

The possible modifications on the microscopic scale induced by the presence of the graphite or by irradiation should have some effect on the vibrational state of the chemical bonds of the polymer. We can speak on terms of long range and short range effects. Breaking of the polymeric chain, from place to place, has no dramatically effect on the behavior of the monomers. This breaking leads in the worst case to a new partition of the long chains in many sub chains. However these new structures, the sub chains, contain thousands of monomers, so that from point of view of vibrational modes of the chemical bonds of the monomer they can be regarded as veritable long chains. The motions involving the monomers are not perturbed by this division of the long chain, [11]. In these terms we speak about the long range effect. Raman investigation is not sensitive to such effects. If the radiation produces much dense breaks along one given chain, or even breaking of the chemical bonds of the monomer, then the vibrations of the chemical bonds are affected. This situation can be reflected by the Raman spectrum. We speak on this case about short range effect of the radiation. From the above discussion it results that only short effects can be observed by Raman spectroscopy. In order to observe such effects we compared the spectra of pure PAA membranes before and after irradiation. Before irradiation the most intense bands are observed at 1096 cm^{-1} (assigned to ρ CH_2); 1333 cm^{-1} (assigned to ν COO); 1451 cm^{-1},(assigned to δ CH_2 vibration); 1682 cm^{-1} (assigned to C = O stretching vibration of the cyclic dimmer) and 2931 cm^{-1}, (Fig. 2), [12-14]. No major modifications appear after irradiation.

The characteristic bands of the polymer appear at the same wave numbers without displacement. Only the amplitude of some bands is modified. More important effects can appear after the introduction of the graphite in the polymeric gel. Depending on the concentration of the dopant, the carbon atoms can occupy positions in the vicinity of the monomers. They can perturb the local vibration of the chemical bonds of the atoms in which vicinity they are located.

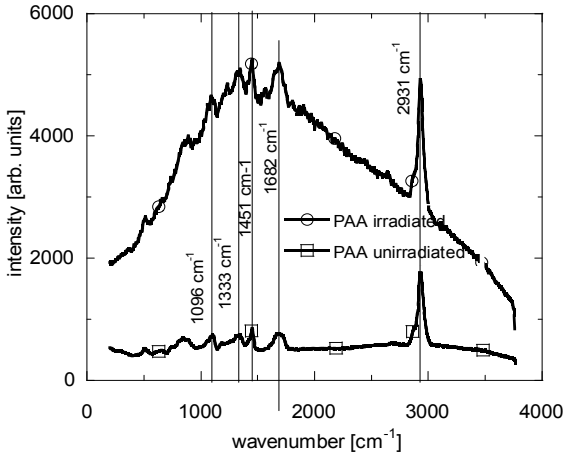

Fig. 2. The Raman spectra of pure PAA membrane before and after irradiation

Such effect is traduced by the displacement of the vibration bands of the concerned chemical bonds. These effects are expected to be seen only at high concentration of the graphite, or in special conditions which should facilitate the attachment of carbon atoms to the polymeric chain. The Raman spectra of PAA membranes including different concentrations of graphite, before irradiation, are shown in figure 3.

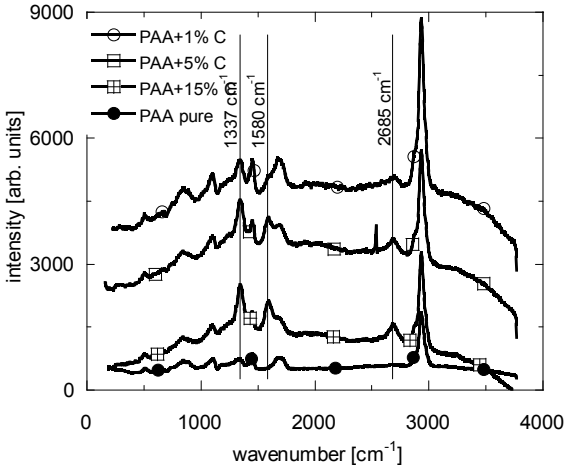

Fig. 3. The Raman spectra of pure PAA membrane and PAA with different concentrations of graphite before irradiation

In these spectra the characteristics bands of the PAA appears at the same wave numbers as for the pure polymer. No shift of these bands can be observed. However these spectra contain supplementary bands belonging to the graphite. The most intense can be observed at 2685 cm^{-1} and 1580 cm^{-1}. The band at 1337 cm^{-1} can be difficult distinguished from the band 1333 cm^{-1} of pure polymer. The amplitude of this band increases with the concentration of the graphite. That means a superposition of the bands of the graphite and pure polymer.

The samples with graphite were investigated also after irradiation. The Raman spectra were compared for each sample before and after irradiation and compared also with the pure polymer. These spectra are presented separately for concentrations 5% graphite in figure 4 and for 15% in figure 5.

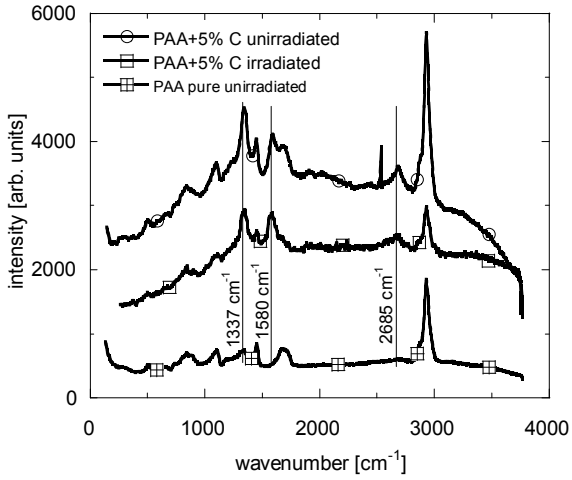

Fig. 4. The Raman spectra of PAA with 5% graphite before and after irradiation, and the spectrum of pure PAA before irradiation

As we can see from these figures the characteristics bands of the polymer and of the graphite appear at the same positions before and after irradiation. Only a weak decrease of the amplitude of the bands appears after irradiation. This effect can be seen for all the concentrations of the graphite, 1%, 5% and 15%. The vibration modes of the chemical bonds of the monomer are not perturbed at this dose of radiation. The vibrational bands appear at the same wave number before and after irradiation, that demonstrate that no chemical bonds appear between the polymer and the graphite. This result reinforces the idea that the graphite is

dispersed in the polymeric, matrix as microscopic bulks without chemical links with the polymer. The electric conduction is determined by the physical contacts established between the domains occupied by the graphite. After irradiation the long range structure of the polymer is perturbed, the distance between the domains occupied by the graphite is modified and thus the number of electric contacts established between the domains occupied by the graphite is affected. That induces modifications of the electric conductivity. So we can explain the electric behavior of the system after irradiation.

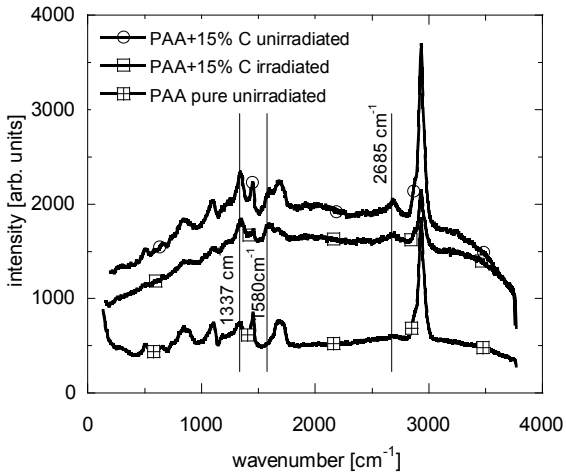

Fig. 5. The Raman spectra of PAA with 15% graphite before and after irradiation, and the spectrum of pure PAA before irradiation

CONCLUSIONS

The possibility to modify the electric conductivity of PAA membranes by inorganic doping and gamma irradiation was tested by electric and Raman measurements. The pure polymeric membranes are characterized by low electric conductivity before and after irradiation. The introduction of small quantities of graphite leads to an important increasing of the conductivity. The resistivity of doped samples decreases continuously with the increase of the concentration of the graphite. No chemical bonds appear between the polymer and the graphite. This fact was proved by Raman investigation. The gamma irradiation of doped samples doesn't affect substantially the electric conductivity. Only a limited effect of breaking of polymeric chains is attributed to the irradiation. This effect is followed

by limited increasing of the local dynamics of the chains with consequences on the modification of the probability of apparition of connections between the domains occupied by the polymer. This effect is associated with the low increasing of the electric conductivity of doped samples after irradiation. The doped samples appear as stables systems at moderate gamma irradiation.

ACKNOWLEDGEMENTS

T. Stefan acknowledges *Investing in people!* Ph.D. scholarship, Project co-financed by the SECTORAL OPERATIONAL PROGRAM FOR HUMAN RESOURCES DEVELOPMENT 2007–2013, Contract nr. **POSDRU/107/1.5/S/76841** – "Innovative doctoral studies in a Knowledge Based Society", Babeş-Bolyai University, Cluj-Napoca, Romania.

REFERENCES

1. R. Chandra, R. Rustgi, *Prog. Polym. Sci*., 23, 1273 (1998).
2. E. Chiellini, A. Corti, S. D'Antone, R. Solaro, *Prog. Polym. Sci.*, 28, 963 (2003).
3. X. Cui, F. Cui, Q. He, L. Guo, M. Ruan and J. Shi, Fuel, 89, 372 (2010).
4. C.-C. Yang, J. Membrane Sci., 288, 51(2007).
5. Timar-Gabor A, Ivascu C, Vasiliniuc S, Daraban L, Ardelean I, Cosma C and Cozar O *Applied Radiation and Isotopes* doi: 10.1016/j apradiso 2011.01.015.
6. A.S. Hoffman, *Adv. Drug Del. Rev*. 43, 3 (2002).
7. M. Todica, C.V. Pop, Luciana Udrescu and Traian Stefan, *Chin. Phys. Lett*. 28, 12, 128201-128201-4, (2011).
8. Barbara Stuart, *Polymer Analysis,* (Wiley), 2002.
9. T. Stefan, C. Leordean, C.V. Pop, D. Marconi and M. Todica, Studia UBB Physica, Vol. 57, (LVII), 2, pp. 53-60, (2012).
10. S. Astilean, Metode şi tehnici moderne de spectroscopie optică, (Casa Cărţii de Ştiinţă, Cluj-Napoca), 2002.
11. M. Todica, Luciana Udrescu, *Metode experimentale în fizica polimerilor*, (Presa Universitară Clujeană), 2013.
12. O. Cozar O,N. Leopold, C. Zelic, V. Chis, L. David, A. Pîrnău , M. Tomoaia-Cotisel, *Journal of Molecular Structure*, 788**,** 1 (2006).
13. He Chen, Jiaxing Li, Dadong Shao, Xuemei Ren, Xiangke Wang, *Chemical Engineering Journal*, 210, 475–481 (2012).
14. Dong J, Ozaki Y, Nakashima K, *Macromolecules*, 30, 1111, (1997).
15. V. Chis, M. Burstalan, C. Morari, O. Cozar, L. David, *Journal of Molecular Structure,* 283, 482, (1999).

STUDIA UBB PHYSICA, Vol. 58 (LVIII), 2, 2013, pp. 31-36
(RECOMMENDED CITATION)

COMPOSITIONAL INVESTIGATIONS ON SOME FRUITS COMMERCIALIZED ON ROMANIAN MARKET

ADRIANA DEHELEAN[a,*] AND DANA ALINA MAGDAS[a]

ABSTRACT. The elemental content of plants is mainly related to the geological and pedoclimatic characteristic of the site of growth. Frequently, the heavy metals for which dietary exposure is of interest are present in trace and ultra trace quantities. Hence, an analytical technique with sufficient sensitivity for the accurate determination of these chemicals in fruit samples is represented by ICP-MS. In this work some fruit assortments (apple, plum, cherry, orange, grape and pear) commercialized on Romanian market were investigated from the point of view of their essential elements and toxic elements.

Keywords: *ICP-MS, heavy metals, minerals*

INTRODUCTION

Fruits are an integral part of human diet as they supply vitamins and minerals, the important constituents essential for human health [1]. Diets high in fruits are also linked to decreased risk of diseases (diabetes, cancer, etc.) and their consumption should be encouraged [2]. Beside this, mineral ions are of prime importance in determining the fruit nutritional value. The importance of minerals such as potassium, calcium, sodium etc. to human health is well known and required amounts of those must be in human diet to pursue good healthy life [3].

The effect of heavy metal contamination of fruits cannot be underestimated as these foodstuffs are important components of human diet. The intake of heavy metal-contaminated fruits may pose a risk to human health; hence the heavy metal contamination of food is one of the most important aspects of food quality assurance [4, 5].

[a] *National Institute for Research and Development of Isotopic and Molecular Technologies, 65-103 Donath Street, P.O. Box 700, 400293 Cluj-Napoca, Romania. * Corresponding author: abenta@itim-cj.ro*

Absorption and accumulation of heavy metals in vegetables and fruits are influenced by many factors, including: concentration of heavy metals in soil, composition and intensity of atmospheric deposition, including precipitations, phase of plant vegetation [6]. To all of these, can be added other sources generated by agricultural technologies such as: irrigation with wastewater, the administration of organic and mineral fertilizers with the load of heavy metals, or application of pesticides, which contain in their structure such chemical elements [7]. Although many heavy metals do not play any significant role in the body of plants, metals like copper, zinc and iron are essential elements in the body of the plant due their physiological functions. The essential elements are very important because they are involved in many enzymes systems in the human body but at high concentrations these are toxic [8, 9].

In the present study, the concentrations of essential mineral elements were analyzed: sodium (Na), magnesium (Mg), phosphorous (P), potassium (K), and calcium (Ca), six essential or potentially essential elements: manganese (Mn), iron (Fe), cobalt (Co), nickel (Ni), copper (Cu), and zinc (Zn), as well as toxic elements: chromium (Cr), arsenic (As), cadmium (Cd), mercury (Hg) and lead (Pb) in different types of fruits available in market from Romania. The fruit samples were analyzed using Inductively Plasma Mass Spectrometry (ICP-MS). The concentrations of metals found in all fruits were compared with the recommendable allowable limits by World Health Organization [10] in drinking water.

EXPERIMENTAL

The samples were firstly oven-dried at 80°C for 3 days. The dried samples were then powdered manually in a grinder and were subjected to the compositional analysis by Inductively Coupled Plasma Mass Spectrometry. The majority of ICP-MS applications involve the analysis of aqueous samples, directly or following sample pretreatment, because of the advantages of working with samples in solution. To avoid the clogging of the nebulizer, fruit samples were diluted. For digestion of fruit samples, 2.5 ml of ultrapure HNO_3 were added to 2.5 ml of sample in a Teflon receptacle, tightly closed. Six such receptacles were inserted in a device made of six stainless steel cylinders mounted between two flanges, to confer pressure resistance. The whole system was put in an oven at 180°C for 12 hours. A colorless solution resulted, and ultrapure water was added up to 50 ml. Thus, the fruit samples were diluted 1:20 v/v. The analysis was performed using a semi-quantitative method available with Perkin-Elmer ICP-MS instrumentation (e.g., Perkin–Elmer Total Quant III). A Perkin Elmer ELAN DRC (e) instrument was

used with a Meinhart nebulizer and silica cyclonic spray chamber and continuous nebulisation. The following instrumental parameters of Elan DRC-e spectrometer were used: 0.97 l/min Nebulizer Gas Flow (NEB), 1.2 l/min Auxiliary Gas Flow, 15 l/min Plasma Gas Flow, 1100 W ICP RF Power, CeO/Ce=0.027, Ba^{++}/Ba=0.025.

RESULTS AND DISCUSSION

Fruits bring an important contribution of minerals to the healthy life of humans. Depending of the fruit type, the contribution of a certain nutrient is different in each fruit. From this point of view, knowledge about the major nutrient content of each type of fruit should be familiar. Besides all benefits brought by the fruits consumption, the ingestion of some toxic metals within these could occurs. Heavy metals like: As, Cr, Cd i.e. naturally occur in fruit composition due to some specific agricultural practices or to pollution issues.

The present study reports the composition of: macro minerals (Na, Mg, P, K and Ca) (Table 1), essential or potentially essential elements (Mn, Fe, Co, Ni, Cu and Zn) (Table 2) and toxic elements (Cr, As, Cd, Hg and Pb) (Table 3) determined in selected fruits from Romanian market.

Table 1

Concentration of macro minerals in fruit analyzed

Sample	Concentration [µg/l]				
	Na	Mg	P	K	Ca
apple	901.92	12618.08	77993.90	434432.06	470390.98
plum	1326.46	66171.08	77537.64	1265440.04	71656.82
cherry	1388.94	10043.24	50295.52	382463.40	7937.06
orange	2758.04	89833.54	173998.90	1040441.40	124812.90
grape	3076.58	49833.40	107005.18	884661.92	106165.52
pear	2110.46	39028.46	92313.28	824879.4	39380.22

The concentrations of Na ranged from 901.92 µg/l (in apple fruit) to 3076.58 µg/l (in grape fruit), while the concentrations of K was between 382463.40 µg/l (in cherry fruit) and 1265440.04 µg/l (in plum fruit). Though the concentration of Mg ranged from 10043.24 µg/l (in cherry fruit) to 89833.54 µg/l (in orange fruit), that of P ranged from 50295.52 µg/l (in cherry fruit) to 173998.90 µg/l (in orange fruit). The concentration of Ca varied between 7937.06 µg/l (in cherry fruit) and 470390.98 µg/l (in apple fruit).

It could be observed that the highest concentration of Ca was obtained for the apple sample while the orange fruit was characterized by the highest contents of Mg and P. The maximum level of Na was detected in the grape sample and the highest content of K was obtained for the plum sample. Also, the lowest concentrations of macro minerals (Mg, P, K and Ca) were observed in cherry fruit.

Table 2

Concentration of essential or potentially essential metals in fruit analyzed

Sample	Concentration [µg/l]					
	Mn	Fe	Co	Ni	Cu	Zn
apple	108.16	844.46	0.62	10.56	147.06	127.26
plum	357.38	643.24	1.92	81.62	550.88	736.44
cherry	107.12	155.74	0.80	42.98	84.16	91.22
orange	286.36	659.70	6.90	128.72	285.54	481.16
grape	576.00	2614.72	2.06	60.58	605.58	389.24
pear	245.42	4218.26	8.64	180.42	712.96	340.04
WHO2008	*400*	**No guideline*	*Not mentioned*	*70*	*2000*	***No guidline*

*No Guideline, because it is not of health concern at concentrations normally observed in drinking water, but may affect the acceptability of water at concentration above 300 µg/L

**No Guideline, because it occurs in drinking water at concentrations well below those at which toxic effects may occur

From Table 2 we observe that the fruit which contained the highest amount of Fe is the pear while the cherry sample is characterized by lowest contents of: Fe, Mg and P from all studied samples.

Table 3

Concentration of toxic elements in fruit analyzed

Sample	Concentration [µg/l]				
	Cr	As	Cd	Hg	Pb
apple	35.44	0.88	0.24	<DL	9.76
plum	32.14	0.72	0.66	0.80	9.96
cherry	42.34	0.04	0.32	0.21	1.08
orange	86.50	0.30	<DL	<DL	2.36
grape	189.44	1.36	0.54	0.20	22.76
pear	122.46	2.96	7.36	1.38	14.4
WHO 2008	*50*	*10*	*3*	*1*	*10*

Table 3 presents the toxic elements concentrations of investigated fruits. Knowing, the toxic element content is very important because some of them are extremely dangerous for human health. For instance, the toxicity of inorganic and organic As compounds has been of global concern because of their probable role in promoting cancer of the bladder, lung, skin, and prostate in humans, among others [11]. Cadmium is a highly toxic metal with a natural occurrence in soil, but it is also spread in the environment due to human activities [12]. Lead is another wide spread toxic pollutant which has no known functions in biological systems. The major source of environmental lead is metal smelting, but agriculture, industry, and urban activities are also important sources of Pb pollution [13].

Our results about essential or potentially essential elements for selected fruits, purchases from Romanian market, are compared with recommended drinking water standards imposed by international organization World Health Organization (WHO). Also, the determined concentrations of Cr, As, Cd, Hg and Pb from fruits were compared with the imposed limit by WHO in 2008, in order to know the levels of fruits contamination with toxic metal.

The concentration of As, Cd, Pb and Cr may be an indication of degree of pollution in the area where the fruit was obtained or degree of absorption of these metals by the plant root. High concentrations of these elements in grape and pear samples may be due to the high degree of pollution in the area from which the fruit was harvested.

Generally, the essential or potentially essential elements concentrations are within the upper limits set by WHO, except Mn (for one sample) and Ni (for two samples). The performed measurements on selected fruits revealed the presence of toxic metals like: Cr, Cd, Hg and Pb concentrations which exceed the WHO imposed limits for some samples: orange, grape and pear.

CONCLUSION

Investigated fruits were purchases from Romanian market and were analyzed from the point of view of their essential and toxic elements using ICP-MS method. The high content of Ca, Mg, P, K, Co, Cu, Fe and Mn demonstrate the nutrient potential of investigated fruits, these being an important source of essential nutrient elements. Knowing the concentration of macro minerals in different fruits is of great importance because in this way we are able to choose the fruits that we are consuming in function of our personal needs. In this context, we observed that the highest content of Ca was found in apple; meanwhile the concentrations of Mg and P had a maximum for the orange sample. The plum sample posses the biggest quantity of K and the maximum level of Na was found in the grape sample.

On the other hand, the allowable limits for some toxic metals: Cr (for orange, grape and pear fruit), Cd (for pear fruit), Hg (for pear fruit) and Pb (for grape and pear fruit) imposed by World Health Organization, were exceeded.

ACKNOWLEDGMENT

This work was supported by the PN II (2007–2013) Program Contract no. 120/2010.

REFERENCES

[1]. O. Mumzuroglu, F. Karatas and H. Geekil, *Food Chem*., 83, 205-212 (2003).
[2]. P. Leterme, *British Journal of Nutrition*, 88 (Suppl. 3), S239-S242 (2002).
[3]. B. San, A.N. Yildirim, T.M. Pola and F. Yildirim, *Asian J. of Chem*. 21(4), 2898-2902 (2009).
[4]. M.A. Radwan and A.K. Salama, *Food and Chemical Toxicology*, 44, no. 8, 1273-1278 (2006).
[5]. M.A. Elbagermi, H.G.M. Edwards, and A.I. Alajtal, *Analytical Chemistry*, 2012, ID 827645, *http://dx.doi.org/10.5402/2012/827645*, (2012).
[6]. R. Lăcătuşu, A.R. Lăcătuşu, *Carpth. J. of Earth and Environmental Sciences*, 3, no. 2, 115-129 (2008).
[7]. K.P. Singh, D. Mohou, R. Dalwani, *Chemosphere*, 55, 227-255 (2004).
[8]. D.M. Miller and W.P. Miller. "Land application of waste", Summer M.E. (ed) Handbook of soil science CRC Books New York, 2000.
[9]. J.K Tufuor, J.K. Bentum, D.K. Essumang, J.E. Koranteng-Addo, *J. Chem. Pharm. Res*. 3(2), 397-402 (2011).
[10]. WHO, "Guidelines for drinking water quality", World Health Organization, Geneva. ISBN 978 92 4 154761 1 (WEB version) (NLM classification: WA 675), 2008.
[11]. R.J. Peralta-Videa, M.L. Lopez, M. Narayan, G. Saupe, J. Gardea-Torresdey, *The International Journal of Biochemistry & Cell Biology,* 41, 1665-1677 (2009).
[12]. I.J. Cindric, I. Krizman, M. Zeiner, Š. Kampic, G. Medunic, G. Stingeder, *Food Chemistry*, 135, 2675-2680 (2012).
[13]. L. Marchiol, S. Assolari, P. Sacco, G. Zerbi, *Environ. Pollut*., 132, 21-7 (2004).

STUDIA UBB PHYSICA, Vol. 58 (LVIII), 2, 2013, pp. 37-51
(RECOMMENDED CITATION)

THE CORROSION BEHAVIOUR OF Zn LAYERS, ELECTRODEPOSITED ON DIFFERENT SUBSTRATES, BY IMPULSE ELECTROPLATING AND BY ELECTRODEPOSITION UNDER MAGNETIC FIELD METHODS

MIHAIL CHIRA[a,*], HORATIU VERMEŞAN[a], VASILE RUS[a], ERNEST GRUNWALD[b]

ABSTRACT. The Zn layer was electrodeposited on various substrates by using various electrodepositing methods. The layers corrosion behavior in 1% NaCl solution was measured by potentiodynamic method and by electrochemical impedance spectroscopy method. The coatings corrosion resistance is influenced both on the depositing method and on the substrate nature, respectively.

Keywords: *zinc, corrosion, magnetic field, impedance spectroscopy*

1. INTRODUCTION

Zinc electrodeposition is being used worldwide since the beginning of ’70s, as a first protective coating, mainly in automotive industry [1].

Zinc, as a sacrifice coating on ferrous materials, ensures corrosion protection in normal environment conditions; however, the increasing corrosion resistance requirements have led to research of better performance standards in metal finishing industry [2]. In order to obtain a better anticorrosion performance, thicker zinc layers have been used – up to 25 μm [3], solution that proved to be uneconomic [4]. Even the olive-green zinc passivated thick coatings how weak corrosion resistance and is costly [5]. The major disadvantage of a thick coating is its deformability and poor welding properties. Also, a thick coating shows difficulties during finishing process after painting [6]. The zinc coatings’ micro and microcrystalline structure depends on the bath electrolytes and parameters. The

[a] *Technical University of Cluj-Napoca, Romania, * Corresponding author: mihai2706@yahoo.com*
[b] *SC BETAK SA Bistrita, Romania.*

zinc coating protects as a physical barrier and also cathodically [7]. It works as a sacrifice anode, thus cathodically protecting the iron; however, it rapidly corrodes. The zinc coatings on ferrous substrate corrosion resistance can be improved by alloying zinc with metals or by using non-conventional electrodeposition methods (impulse electroplating, or electrodeposition under magnetic field).

Impulse electroplating is a method to obtain thin films by using high concentration composite particles, and it allows the control of deposition (film composition, thickness, film uniformity, coating rugosity) by impulse amplitude control and width variation.

Impulse electroplating determines the nano-composites structure and morphology and the average size of the crystallites, by varying the current density and based on the growing mechanism [8].

Electrochemical impedance spectroscopy is used for the coatings corrosion behavior study, giving information regarding the electrode capacity, the electric charge transfer kinetics, and the reaction mechanism.

The aim of this work is the study of the zinc coating corrosion behavior, when zinc is deposited on various substrata, by impulse electroplating method, by electrodeposition under magnetic field method and by combination of these two methods, and the comparison with the corrosion behavior when conventional deposition method is used.

2. MATERIALS AND INVESTIGATION METHODS

2.1. Samples

Experiments have been performed at Corrosion and Corrosion Protection Laboratory of Technical University of Cluj-Napoca, Romania.

The substrate used for electrodeposition was 12 cm^2 carbon steel laminated square sheets. The samples were polished with 1500 granulation sandpaper. After polishing, the samples were degreased in 10% NaOH solution, then washed, pickled in HCl (37%) 1:1 solution, and again washed.

In order to improve corrosion resistance it was attempted an intermediate layer, with a diode-like behavior, with the aim to reduce the corrosion resistance close to zero. Thus, 8 samples were immersed for 2 minutes in Na_2SiO_3 solution, then for 3 minutes in HCl (37%) 1:1 solution, thus obtaining a SiO_2 layer on the steel surface.

After being washed, a boron nitride (BN) layer was electrodeposited on 4 of the 8 samples, with the aim to impurify the silicon with trivalent boron. Electrochemical deposition of boron nitride was made by using the sample as anode, while the cathode was stainless steel [9].

Finally, the substrat/sublayers were chosen as following: *steel* (S235JR); *steel/silicon dioxide* (SiO_2) and *steel/silicon dioxide* (SiO_2)/*boron nitride* (BN). The Zn was electrodeposited using 4 methods: 1) conventional electrodeposition (**Zn**); 2) Impulse electroplating method (**Zn+f**); 3) electrodeposition under magnetic field, with the field lines parallel with the sample surface (**Zn+bp**), and 4) Impulse electroplating and electrodeposition under magnetic field, with the field lines parallel with the sample surface (**Zn+bp+f**).

The electrolytes composition for zinc electrodeposition and for boron nitride (BN) deposition is shown in Tables 1 and 2.

Table 1

Electrolyte composition for zinc electrodeposition

$ZnCl_2$	75 g/l
KCl	225 g/l
H_3BO_3	26 g/l
Zeta PLUS 450 BASE (brightening agent)	25 g/l
Zeta PLUS 450 BRILL (brightening agent)	1 g/l
Current density	1.2 A/dm^2
Temperature	20-25°C
Anode	Zinc
Cathode linear oscillation	10 oscillation/min

Table 2

Electrolyte composition for boron nitride electrodeposition (BN)

H_3BO_3	100 g/l
$HCON(CH)_2$	100 g/l
Current density	1.5 mA/cm^2
Temperature	20-25 ^{0}C
Cathode	Stainless steel
Anode-Cathode distance	10 mm

A rectangular impulses generator with 25ms pulse duration (T_{on}=10 ms and T_{off}=15 ms) was used for the impulse electroplating method.

During the electrodeposition under magnetic field method, the samples were submitted to a 70 mT magnetic field, with the field lines parallel with the sample surface.

The following samples notations were used:

1) **(Zn)**–zinc conventionally electrodeposited (ZCE) on steel;
2) **(Zn+f)** –zinc impulse electroplated (ZIE) on steel;
3) **(Zn+bp)**–zinc electrodeposited under magnetic field on steel;

4) **(Zn+bp+f)**– ZIE and electrodeposited under magnetic field on steel;
5) **(Si+Zn)**– ZCE on steel/silicon dioxide;
6) **(Si+Zn+f)**– ZIE on steel/silicon dioxide;
7) **(Si+An+bp)** – zinc electrodeposited under magnetic field on steel/silicon dioxide;
8) **(Si+Zn+bp+f)** – ZIE and electrodeposited under magnetic field on steel/silicon dioxide;
9) **(Si+BN+Zn)** –ZCE on steel/silicon dioxide/boron nitride;
10) **(Si+BN+Zn+f)** – ZIE on steel/silicon dioxide/boron nitride;
11) **(Si+BN+Zn+bp)** – zinc electrodeposited under magnetic field on steel/silicon dioxide/boron nitride;
12) **(Si+BN+Zn+bp+f)** – ZIE and electrodeposited under magnetic field on steel/silicon dioxide/boron nitride.

2.2. Corrosion testing

2.2.1. Potentiodynamic polarisation tests

Potentiodynamic polarisation tests have been performed to find the Zn layer corrosion rate. A Voltalab 10 potentiostat was used. The Tafel anodic (β_a), the and cathodic (β_c) slopes, and the current density were calculated at a potential scanning rate of 10 mV/s,in the range from +200mV to -200mV, relative to the open circuit potential.

2.2.2. Electrochemical impedance spectroscopy (EIS) measurements

In order to measure the EIS, the samples were immersed in 1% NaCl solution. The electrochemical cell contained a reference electrode (Ag/AgCl), a platinum auxiliary electrode, and as a working electrode the sample (with a 0.785 cm^2 surface). The impedance was calculated by the open circuit potential method, using a Voltalab 10 equipped with a frequency response analyzer. The EIS measurements were made under a frequency range from 100 kHz to 1 MHz, with a sinusoidal potential of 10 mV amplitude. The impedance spectra were analyzed using the soft ware connected to the potentiostat.

3. RESULTS AND DISCUSSIONS

3.1. The potentiodynamic polarisation study

The Tafel curves of the potentiodynamic tests are shown in Figures 1, 2 and 3.

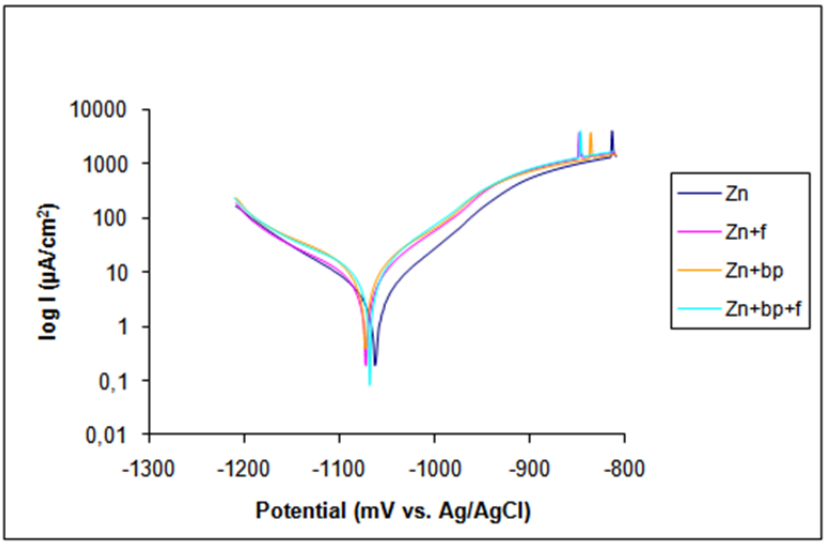

Figure 1. Polarisation curves for samples in 1% NaCl solution, for zinc electrodeposited on steel by the four above-mentioned methods.

The electrochemical parameters corresponding to Figure 1 are shown in Table 3.

Table 3

The zinc layer corrosion rate in 1% NaCl solution, at 25±1°C, for samples of zinc layer electrodeposited on steel by using the four methods.

SAMPLE	β_a *[mV/decade]*	β_c *[mV/decade]*	R_p *[kΩcm²]*	*E(i=0) [mV]*	i_{cor} *[μA/cm²]*
Zn	71.5	-96.1	4.10	-1066.5	3.6654
Zn+ f	76.3	-113.1	2.33	-1076.9	6.4805
Zn+ bp	94.4	-131.0	1.64	-1077.0	11.3402
Zn+bp+f	77.5	-130.6	1.70	-1073.4	9.4217

The conventionally electrodeposited zinc layers and the impulse electroplating zinc layers shown lower current densities compared to those of the samples obtained by using the other electrodeposition methods. Also, the Tafel anode and cathode slopes of the conventionally electrodeposited samples are smaller compared to the other samples. This result shows that the conventionally electrodeposited zinc layer has a higher activation energy compared to the other samples.

The curves corresponding to the zinc layer electrodeposited on steel/SiO_2 substrate by the four methods, and the quantitative data, are shown in Figure 5 and in Table 4, respectively.

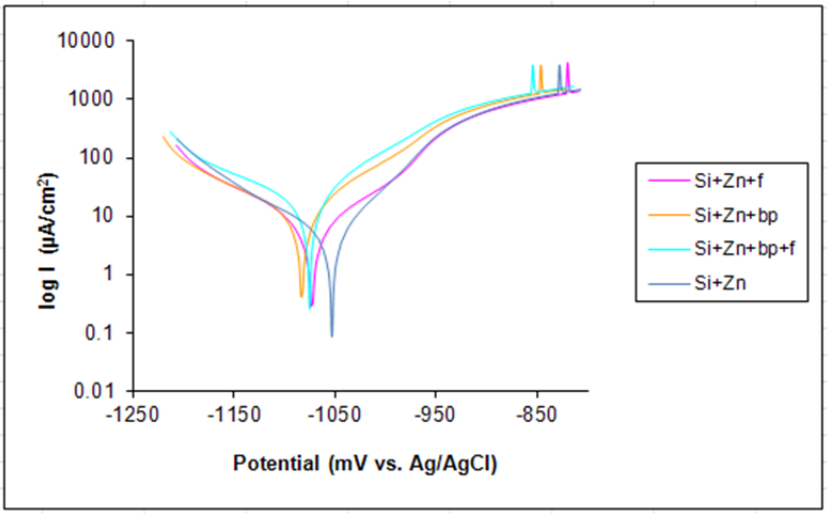

Figure 2. Polarisation curves for samples in 1% NaCl solution, for zinc layer electrodeposited on steel/$SiO_2$by using the four above-mentioned methods.

Table 4

Zinc layer corrosion rate in 1% NaCl solution, at 25±1°C, for samples of zinc electrodeposited on steel/SiO_2 by using the four methods

SAMPLE	β_a *[mV/decade]*	β_c *[mV/decade]*	R_p *[kΩcm²]*	*E(i=0) [mV]*	i_{cor} *[µA/cm²]*
Si+ Zn	59.9	-102.6	3.01	-1058.1	4.2234
Si+ Zn+f	92.9	-104.3	2.76	-1077.3	5.7020
Si+ Zn+bp	62.0	-91.4	1.67	-1087.5	7.0689
Si+ Zn+bp+f	60.5	-100.5	1.05	-1080.2	11.7836

According to Figure 2 and Table 4, it can be seen that the conventionally electrodeposited samples have a lower current density compared to the other samples, while the anodic Tafel slope of this sample is lower than those of the others. This results show that the conventionally electrodeposited zinc layer has a higher activation energy compared to those of the other samples.

The Tafel curves and quantitative data of the zinc layer electrodeposited on steel/SiO_2/BN substrate by using the four electrodeposition methods are shown in Figure 3 and in Table 5, respectively.

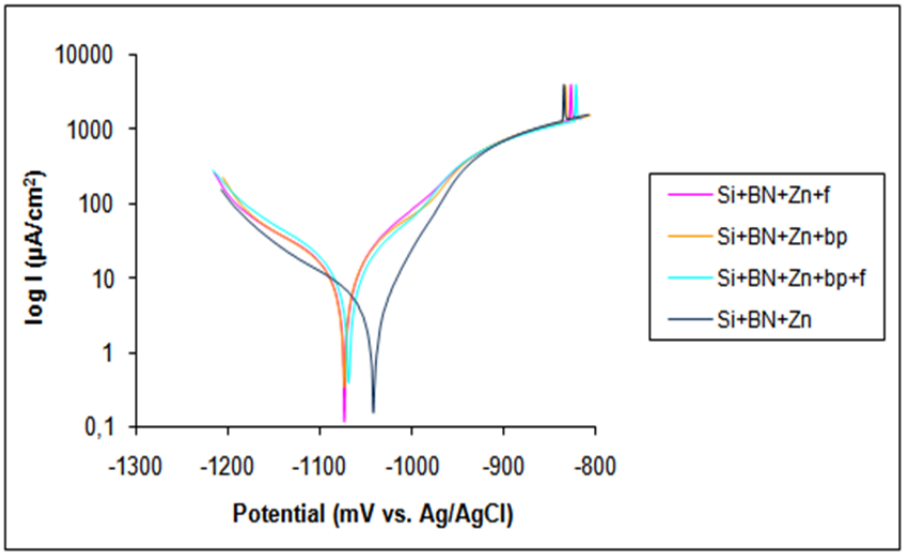

Figure 3. Polarisation curves for samples in 1% NaCl solution, for zinc electrodeposited on steel/SiO_2/BN by using the four above-mentioned methods.

Table 5

Zinc layer corrosion rate in 1% NaCl solution, at 25±1°C, for samples with zinc electrodeposited on steel/$SiO_2$by using the four methods.

SAMPLE	β_a *[mV/decade]*	β_c *[mV/decade]*	R_p *[kΩcm²]*	*E(i=0) [mV]*	i_{cor} *[μA/cm²]*
Si+BN+Zn	43.5	-78.2	3.43	-1046.3	2.7743
Si+BN+Zn+f	86.9	-142.9	1.46	-1078.5	12.5114
Si+BN+Zn+bp	69.6	-93.6	1.45	-1079.2	8.5503
Si+BN+Zn+bp+f	66.2	-66.6	5.16	-1094.4	2.1183

As seen in Table 5, the current densities of (Si+BN+Zn+bp+f) and (Si+BN+Zn) samples are lower compared to those of the other samples, and their anode and cathode Tafel slopes are lower compared to those of the (Si+BN+Zn+f) and (Si+BN+Zn+bp) samples. This result shows that the *impulse electroplated* samples and the zinc *electrodeposited under magnetic field* samples have an activation energy higher compared to that of the other samples.

The electrochemical parameters data of the best corrosion resistance results are compiled in Table 6.

Table 6.

Zinc layer corrosion rate in 1% NaCl solution, at 25±1°C, of samples with zinc electrodeposited on steel, on steel/SiO_2 and on steel/ SiO_2/BN, by using the four methods

SAMPLE	β_a *[mV/decade]*	β_c *[mV/decade]*	R_p *[kΩcm²]*	*E(i=0) [mV]*	i_{cor} *[μA/cm²]*
Zn	71.5	-96.1	4.10	-1066.5	3.6654
Si+Zn	59.9	-102.6	3.01	-1058.1	4.2234
Si+BN+Zn+bp+f	66.2	-66.6	5.16	-1094.4	2.1183

According to Table 6, the (Si+BN+bp+f) sample corrosion current is lower compared to that of the (Zn) sample, which is also lower than that of the (Si+Zn) sample. Also, as seen in the Tafel anode and cathode slopes analysis, the (Si+BN+Zn+bp+f) sample has higher zinc activation energy, and thus, a better corrosion resistance. Even though the polarisation resistances of the three samples have similar values, the corrosion rates vary.

We can conclude that the zinc layer corrosion resistance studied depends on the electrodeposition method used and on the electrodeposition substrate – the sample of zinc coated on steel/SiO_2/BN substrate by the *impulse electroplating and electrodeposition under magnetic field* method, shows the best corrosion resistance.

3.2. EIS study

The Nyquist diagrams for the samples obtained by zinc electrodeposition on steel, on steel/SiO_2 and on steel/SiO_2/BN, are shown in Figure 4.

The Nyquist impedance diagrams for the (Zn) and for the (Si+Zn) samples are similar, looking like flattened semi-circles, due to a constant dispersion with time, and showing an inductive area at low frequencies due to adsorption and to oxide layer growing.

The Nyquist diagram of the (Si+BN+Zn+bp+f) sample looks like a semi-circle that opens at lower frequencies; the process being controlled by diffusion and by electric charge transfer.

The semi-circles diameters are proportional with the film polarisation resistance R_p and with the corrosion rate.

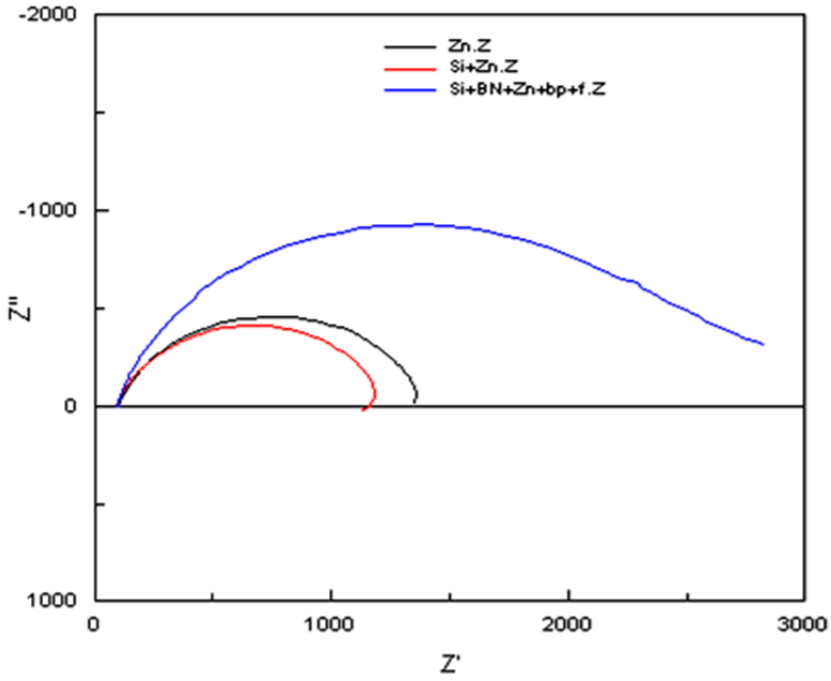

Figure 4. The Nyquist diagrams

The correct interpretation of the electrochemical impedance diagrams and the finding of an equivalent circuit, depend on the corrosion phenomena at the samples surface. According to Suzuki [12] and Chung et al. [10], one of the cathode reactions at the zinc coated sample surface in the ion chlorine environment (SCE), is the dissolved oxygen reduction reaction:

$$\frac{1}{2}O_2 + H_2O + 2e^- \rightarrow 2OH^-$$

This reaction leads to a local increase of pH at the zinc layer surface. The hydroxide film is a base for growing corrosion products [10]. Corrosion products can be chemical compounds as the following: ZnO, $Zn(OH)_2$, $ZnCO_3$, $Zn_5(OH)_6(CO_3)_2$ and $Zn_5(OH)_8Cl_2 \cdot H_2O$; and probably a mixture of these compounds [11]. According to Branco at al. [11] the zinc corrosion products precipitate on the surface exposed to the sodium chloride solution, due to their low solubility. The film formed on the surface is not an ideal layer and is not compact. The film compactness and protective properties depend on the composition and the synthesis conditions [12]. The corrosion products (pores) influenced the electrochemical response at low

frequencies [13].According to Yadav et al [14] the zinc corrosion products stability in chlorine solution depends on the $Cl^-$and H^+ ions concentration, as well as on the corrosion products concentration ($Zn(OH)_2$, $ZnCl_2{\cdot}6Zn(OH)_2$ and $ZnCl_2{\cdot}4Zn(OH)_2$) in chlorine solution [12,14]). The corrosion products chemical reactions are:

$$7ZnCl_2 \cdot 4Zn(OH)_2 + 4H_2O \rightarrow 5ZnCl_2 \cdot 6Zn(OH)_2 + 4H^+ + 4Cl^-$$

$$ZnCl_2 \cdot 6Zn(OH)_2 + 4H_2O \rightarrow 7Zn(OH)_2 + 2H^+ + 2Cl^-$$

According to the above two reactions, the chemical stability of the corrosion products increases with the Cl^- and H^+ ions concentration. According to Yadav et al [14], the $ZnCl_2{\cdot}4Zn(OH)_2$ corrosion product obtained at low pH has a porous structure. This porous corrosion product does not seem to act as a barrier layer for the O_2 and Zn^{2+} transportation – thus corrosion continues. On the other hand, according to Giridhar and van Ooij [15], the pH increase leads to the surface passivation.

The equivalent circuit for the electrochemical impedance corresponding to the steel/Zn and steel/SiO_2/Zn samples is shown in Figure 5.

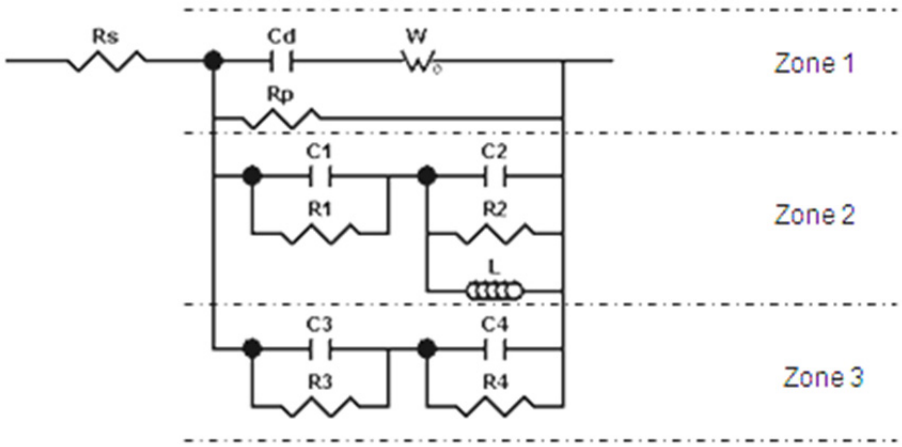

Figure 5. Equivalent circuit for the Nyquist diagrams interpretation,

The equivalent circuit for the electrochemical impedance corresponding to the (Si+BN+Zn+bp+f) sample is shown in Figure 6.

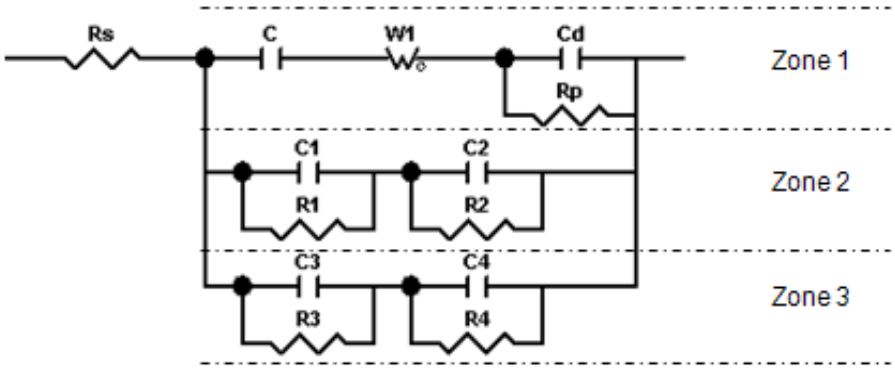

Figure 6. The equivalent circuit for the (Si+BN+Zn+bp+f) sample for the Nyquist diagram interpretation.

There are three areas on the sample surface (randomly distributed on the sample surface) corresponding to the three branches of the circuit, showing various behaviors.

The double electric layer thickness (d_d), the oxide layer thickness (d_1+d_2) and (d_3+d_4) and the diffusion length (L_1),calculated using the capacitor formula ($C = \varepsilon_0\varepsilon_r S/d$) and the Warburg impedance formula ($W\text{-}T = L^2/D$), are shown in Table 7, while the equivalent resistances are shown in Table 8.

According to Tables 7 and 8, in the case of the zinc layer conventionally electrodeposited on steel sample, the Zn^{2+} ions diffuse in solution in the first area, characterized by Warburg impedance (W). The Zn^{2+}ions in the solution, close to the surface at a distance (d_d), determine an electric double layer capacity (C_d) and a polarisation resistance (R_p). A thin oxide layer with thickness (d_1), electric capacitance (C_1) and resistance (R_1) forms in the second area. Supplementary, a porous oxide layer with corrosion products also form (the area of the oxide layer growth).In this region the transfer of electric charge from the solution to the surface, is characterized by an inductance(L), a capacity (C_2) and a resistance (R_2). In the zone 3 there is an oxide layer of (d_4) thickness, with capacity (C_4) and a resistance (R_4). This oxide layer is thicker than that of the second area and is followed by a bipolar water molecules layer of capacity(C_3) and polarisation resistance (R_3). Even though the third area oxide layer has a thickness (d_4) much bigger than that of the second area (d_1), its electric resistance is lower, which lead to the supposition that it is porous (figure 7).

Table 7.

Parameters that characterize the double electric layer thickness (d_d), diffusion length (L_1), the thickness of the oxide layer formed in the second area (d_1), the porous oxide layer thickness and the oxide thickness in the second area (d_2), the oxide layer thickness in the third area and the distance between the capacitor "plates" formed by the water molecules on the third area oxide ($d_3$and d_4)

Sample	d_d *[Å]*	L_1 *[Å]*	d_1 *[Å]*	d_2 *[Å]*	d_3 *[Å]*	d_4 *[Å]*
Zn	2.5	547	1.87	105	2.01	31
Si+Zn	21.76	380	1.84	83	2.15	20.23
Si+BN+Zn+bp+f	66.4	595	25	1.93	7.2	2.79

Table 8.

Solution resistance (R_s), polarisation resistance (R_p), second area oxide resistance (R_1), third area oxide resistance (R_3) and polarisation resistances caused by the water molecules on the oxides surfaces, in the second and third area respectively (R_2, R_4).

Sample	R_s *[Ωcm²]*	R_p *[Ωcm²]*	R_1 *[Ωcm²]*	R_2 *[Ωcm²]*	R_3 *[Ωcm²]*	R_4 *[Ωcm²]*
Zn	127.3	2900	6400	1200	2200	5800
Si+Zn	127.8	2000	6200	2600	5200	4000
Si+BN+Zn+bp+f	95.74	4661	5500	680	5500	680

According to Tables 7 and 8, in the case of the conventionally zinc electrodeposited on *steel/silicon dioxide*, Zn^{2+} ions diffuse in solution in the first area, characterized by Warburg (W) impedance. The Zn^{2+} ions in solution, at the (d_d) distance from the surface, determine an electric double layer of capacity (C_d) and a polarisation resistance (R_p). An oxide film of (d_1) thickness forms in the second area, with a capacity (C_1) and a resistance (R_1). On this oxide film there forms a porous oxide layer, an area where corrosion products also form (the area of the oxide layer growth). Also, the electric charge transfer from solution toward the surface, described by the circuit with inductance (L), capacity (C_2) and resistance(R_2). The thickness of this layer is small and its resistance is higher compared to the thickness and resistance of the (Zn) sample. This lead to the conclusion that the corrosion products have a higher density in the case of the (Si+Zn) sample. In the third area there is an oxide film of (d_3) thickness (which is thicker compared to the second area thickness), with capacitance (C_3) and resistance (R_3).This oxide film is followed by a dipolar water molecules layer with capacitance(C_4), which determines a polarisation resistance(R_4) (figure 7).

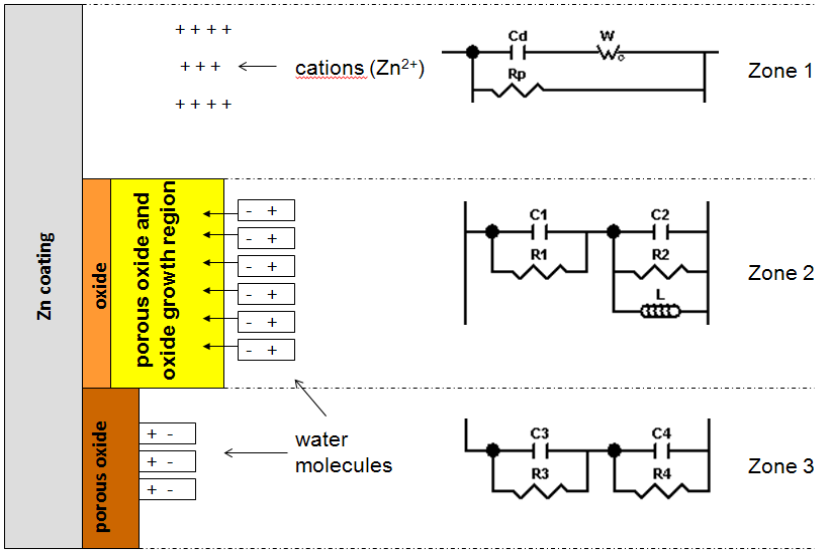

Figure 7. The schematic representation of the three areas and of the circuit branches corresponding to the zinc layer conventionally electrodeposited on steel and the conventionally electrodeposited zinc layer on *steel/silicon dioxide* (Si+Zn).

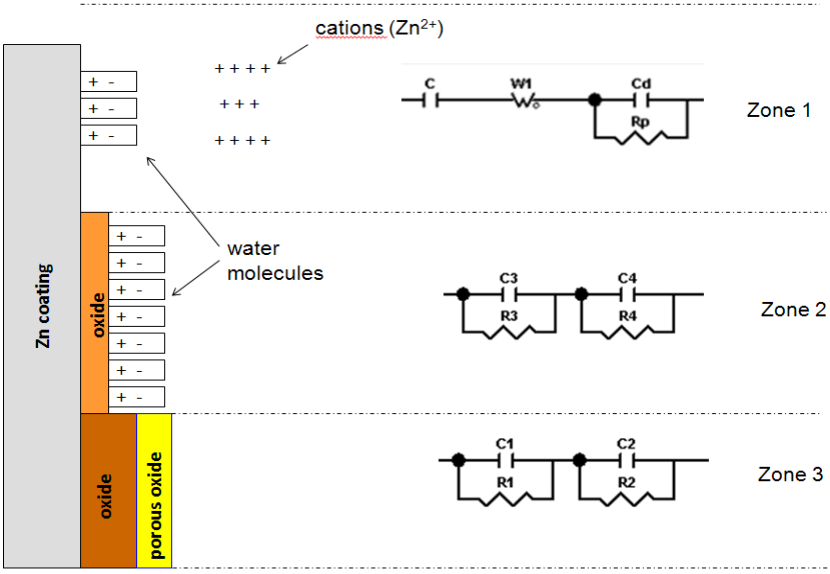

Figure 8. Schematic representation of the three areas and of the circuit branches corresponding to the zinc coating *impulse electroplated/electrodeposited under magnetic field* on *steel/silicon dioxide/boron nitride substrate* (Si+BN+Zn+bp+f).

According to Tables 7 and 8, it was concluded that in the case of the zinc coating *impulse electroplated/electrodeposited under magnetic field* on steel sample, there are water molecules on the first area surface, between the sample surface and the Helmholtz plane, with capacity (C). Also, Zn^{2+} ion diffusion in solution occurs in this area, characterized by Warburg impedance (W).The Zn^{2+}ions in solution close to the surface at a distance (d_d), determine an electric double layer with a capacity (C_d) and a polarisation resistance (R_p). In the second area there is a (d_2) thickness film, with a capacity (C_2) and a resistance (R_2). On this oxide layer there is a large number of water molecules (electric dipoles), which determine a capacity (C_1) and a polarisation resistance (R_1). It was presumed that the dipoles concentration is higher due to the high value of the resistance (R_1). In the third area there is an oxide layer of (d_3) thickness, which is thicker compared to the second area thickness, having a capacity (C_3) and resistance (R_3), followed by an oxide layer of lower density, with a capacity (C_4) and a resistance (R_4) (figure 8).

By comparing the polarisation resistances with the oxide layers resistances for the (Zn), (Si+Zn) and (Si+BN+Zn+bp+f) samples, it was seen that the polarisation resistance of the (Si+BN+Zn+bp+f) sample is higher and the oxide layer is more compact.

The circuit branch formed by the C, W_1, C_d and R_p circuit elements characterizes the active corrosion area, the double electric layer capacity, the polarisation resistance and the diffusion. The circuit branch formed by the C_1, R_1, C_2, R_2, and L circuit elements characterizes the oxide layer formation area, followed by the corrosion products formation area. The circuit branch comprising the C_3, R_3, C_4, and R_4 circuit elements characterizes the oxide layer formation are a followed by the porous oxide layer formation area.

4. CONCLUSIONS

1. The potentiodynamic measurements and the Nyquist diagram show that the zinc layer electrodeposited on *steel/silicon dioxide/boron nitride* by *impulse electroplating/electrodeposition under magnetic field* method has a better corrosion behavior compared to that of the zinc layer obtained by the conventionally electrodeposited method on steel.

2. The corrosion resistance depends on the substrate and on the electro-deposition method used. According to the experimental results for the three sets of samples, the corrosion resistance is influenced by the electrodeposition method, when the same substrate was used. For the same electrodeposition method, the corrosion resistance depend on the nature of substrate.

ACKNOWLEDGMENT

This paper was supported by the project "Improvement of the doctoral studies quality in engineering science for development of the knowledge based society-QDOC" contract no. POSDRU/107/1.5/S/78534, project co-funded by the European Social Fund through the Sectorial Operational Program Human Resources 2007-2013.

REFERENCES

[1]. R. Fratesi, G. Roventi, -Surface and Coatings Technology 82, (1996), p.158.
[2]. Fei Jing-Yin, Liang Guo-Zheng, Xin Wen-Li, Wang Wei-Kang, - Journal of Iron and Steel Research , International. 3(4), (2006), p. 61.
[3]. S.A. Watson, Trans.Inst. Met. Finish. 70 (1992), p.28.
[4]. E. Popesco, TOURNIER, R., Zincarea electrolitică practică, Editura MEDRO,Bucureşti, (1998).
[5]. M. Mortaga, Abou-Krisha, - Applied Surface Science 252, (2005), p. 1035.
[6]. C. Salacruz, P. Bares, J.P. Bonino, C. Muller, M. Sarret, Traitment termique&inginerie des Surface nr. 375 Nov-Dec. (2006), p.55.
[7]. P. Ozga, E. Bielanska, -Materials Chemistry and Physics 81, (2003), p. 562.
[8] T. Frade, V. Bouzon, A. Gomes, M.I. Pereira da Silva CCMM, Surface & Coatings Technology Volume: 204 Issue: 21-22 Pages: 3592-3598 Published: 2010
[9] M. Pal Chowdhury, B.R. Chakraborty, A.K. Pal, Materials Letters 58 (2004) pag. 3362–3367.
[10] S.C. Chunga, J.R. Chengb, S.D. Chioub, H.C. Shiha, Corrosion Science 42 (2000) page: 1249-1268.
[11] V. Barranco, S. Feliu Jr., S. Feliu, Corrosion Science 46 (2004) 2203.
[12] I. Suzuki, Science 25 (1985) 1029-1034.
[13] R.G. Kelly, J.R. Scully, D.W. Shoesmith, R.G. Buchheit, Electrochemical Techniques in Corrosion Science and Engineering, September 13, 2002 by CRC Press - 440 Pages.
[14] A.P. Yadav, A. Nishikata, T. Tsuru, Corrosion Science 46 (2004) 361.
[15] J. Giridhar, W.J. van Ooij, Surface & Coatings Technology 53 (1992) 35.

STUDIA UBB PHYSICA, Vol. 58 (LVIII), 2, 2013, pp. 53-65
(RECOMMENDED CITATION)

AN EXPERIMENTAL AND FINITE ELEMENT ANALYSIS OF MATERIAL FLOW DURING FORWARD EXTRUSION OF LEAD ALLOY

M. POP[a,*], D. FRUNZA[a], C. PAVEL[a]

ABSTRACT. An experimental and finite element analysis (FEA) of forward extrusion of lead alloy were developed. In order to determine the deformation flow patterns, square grids were scribed on the meridional plane of one of the two matching halves of the splitted-lead specimens. A finite element analysis (FEA) of the cold forward extrusion process was undertaken in parallel with the experimental programme. Data obtained from the FE model included extrusion force, effective stress and strain and material deformation flow. The data obtained by numerical simulation confirm theoretical and experimental results.

Keywords*: forward extrusion, die angle, ram speed, metal flow, finite element method*

INTRODUCTION

An important objective of the deformation processing of metals and alloys is the production of defect-free parts, with the desired microstructure and properties. This goal can be achieved by: better design and calculation methods and better control of the parameters of the deformation processes. This should be based on a deeper knowledge of the phenomena that accompany the deformation of material and of the relationships between the properties of the deformed materials and the conditions of deformation.

The progress in computer hardware and simulation tools has, in recent years, enabled complicated simulations of industrial forming processes. However, the accuracy of such simulations will remain dependant on the reliability of the material data, most important of all the true flow stress. Experimental tests at

[a] *Technical University of Cluj-Napoca, Faculty of Materials Science and Environmental Engineering, B-dul Muncii, 103-105 Romania, * Corresponding author e-mail: mariana.pop@ipm.utcluj.ro*

different strains, strain rates and temperatures reached during metal forming application are performed to reveal this constitutive relationship, which relates the deformation behavior to stress.

Extrusion is a bulk forming process in which the material is made to flow using high pressure. The deformation takes places mainly at room temperature in the case of cold extrusion and plate-finished workpieces with close dimensional accuracy are obtained Cold extrusion can be used with materials that has adequate coldworkability, like steel, lead, tin, zinc, copper and alloys. Study of metal flow in extrusion billet is fundamental and useful to understand extrusion technology. Investigation of behavior of extrusion billet skin and microstructure of products were reported by M. Schikorra et al.2008 [1]. The geometrical features of the die land are a critical feature in obtaining defect free cold extruded parts. As the die land length directly influences the amount of friction at the die–billet interface, extrusion die designers use this geometrical parameter to control the metal flow from the die. A physical model capable of predicting the friction and sticking/slipping lengths in the bearing channel during unlubricated aluminium extrusion processes were developed by X. Maa, et. al. 2010 [2]. The influence of die angle, reduction ratio and die land on the extrusion force during the cold extrusion process were investigated by J.S. Ajiboye et al.2006 [3] ,S.O. Onuh, et al.2002 [4] and P. Tiernan, et al. 2005 [5]. Further investigation were developed on the deformation models and internal flow patterns of the deformed specimens by J.S. Ajiboye , et al. 2006 [3] and N.Solomon, et al.2010 [6]. Finite element analysis (FEA) of the cold and hot extrusion process was undertaken in parallel with experimental programme. P. Tiernan et al. 2005 [5] reported data obtained from the FE model included die-workpiece contact pressure, effective stress and strain and material deformation velocity. The relative influences of the semi-angle of the die, the extrusion ratio and the friction factors were examined by Dyi-Cheng Chen et al. 2007 [7]. In order to predict the temperature evolution during the extrusion of aluminium alloys were developed researches by means of 3D FEM computer simulation. Results show that ram speed has a significant influence on the temperature distribution in the billet, which continuously changes throughout the process, as a result of complex heat generation and heat loss as is shown by L. Li et al. 2004 [8].

An experimental and numerical programme of forward cold extrusion was undertaken in the present investigation. The aims of the research were to analyse the effect of some geometrical variables involved in the process, namely, die angle and ram speed on the extrusion force. Also the influence of tehnological parameters on material flow was studied. A finite element analysis of the extrusion process was carried out using MSC SuperForm software in parallel to the experimental programme. Results from the finite element program included extrusion force, effective stress and strain, strain rates and material flow patterns.

THEORETICAL ASPECTS

An important advantage of extrusion is that it produces compressive and shear forces in the billet; no tensile force is produced, which makes high deformation possible [5]. Figure 1 present the forward extrusion principle and the states of stress and strain in the deformation zone.

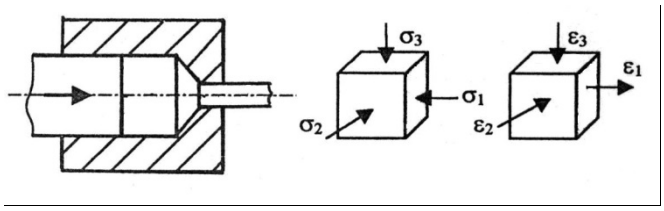

Fig. 1. a.Principle of forward extrusion;
b. State of stress and strain in forward extrusion

A schematic illustration of the forward extrusion is presented in Figure 2.

Recently, the progress in computer hardware and simulation tools led to a wide application of FEM simulations to study the forging process [10,11,12,13,15,16].

Constitutive equations are used to describe the changes in strength observed to occur in materials being deformed. These formulations are empirical and relate changes in strength produced from variation in strain, temperature or strain rate.

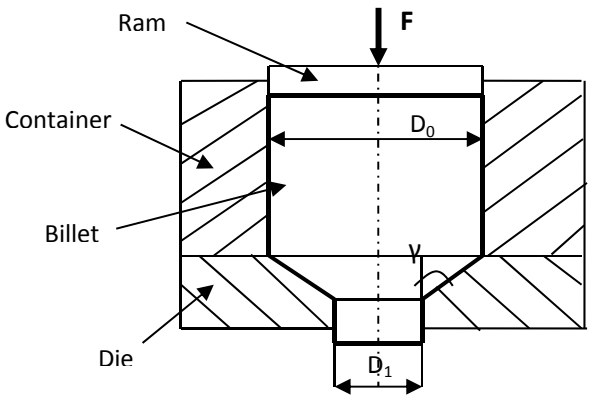

Fig. 2. Schematic illustration of the forward extrusion process

The general form of constitutive equation is:

$$\overline{\sigma} = f(\varepsilon, \dot{\varepsilon}, T, \sigma^*) \tag{1}$$

where: σ , true stress; ε , true plastic strain; $\dot{\varepsilon}$, strain rate; T, temperature; σ^* , parameter dependent of the history of deformation.

In figure 3, is presented the flow pattern specific for forward extrusion in an intermediate stage of the extrusion process. The metal, which at this instant resides in the shear zone and in the secondary deformation zone, sooner or later during continued extrusion will be squeezed into the primary deformation zone. Depending on the alloy extruded, this dead zone will be more or less well developed. The metal of the secondary deformation zone gradually flows into the primary deformation zone. In the peripheral region of the billet, can be identified, the shear zone which deform differently from those in the interior of the billet. When the ram has reached the horizontal line marked A, the secondary deformation zone no longer is present. [18].

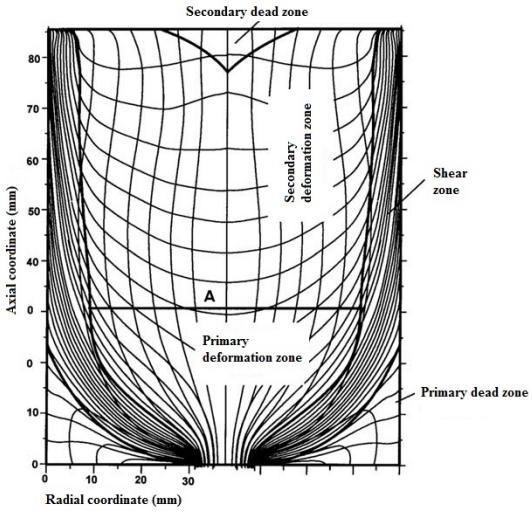

Fig. 3. Forward extrusion with deformed internal grid pattern and zones with different deformation characteristics

EXPERIMENTAL DETAILS

The lead (Pb99,5) samples were used to study the influence of geometrical parameters of the process on the extusion force and material flow pattern. The billets were subjected to upsetting tests on Heckert type hydraulic press with

maximum force of 200KN. The ram speed during the tests were 0,5mm/s, 2 mm/s, 5mm/s. During the experiments, the ram displacement, the time and the upsetting force were recorded simultaneously using a specific data acquisition system.

The three parameters varied during the experimental work were the die exit diameter, *d* , die angle, *α* and the ram speed (0,5 mm/s, 2mm/s, 5 mm/s).

In order to determine the flow curve for lead alloy, torsion tests were carried out, using samples of 9 mm in diameter and 30 mm in lengh. Test were carried out at stain rates between 0,02 [1/s] and 6,6 [1/s] [14].

RESULTS AND DISCUSSIONS

Fig. 4 shows the true stress-strain curve for lead. The obtained values are in accordance to data given by Laue and Stenger [20].

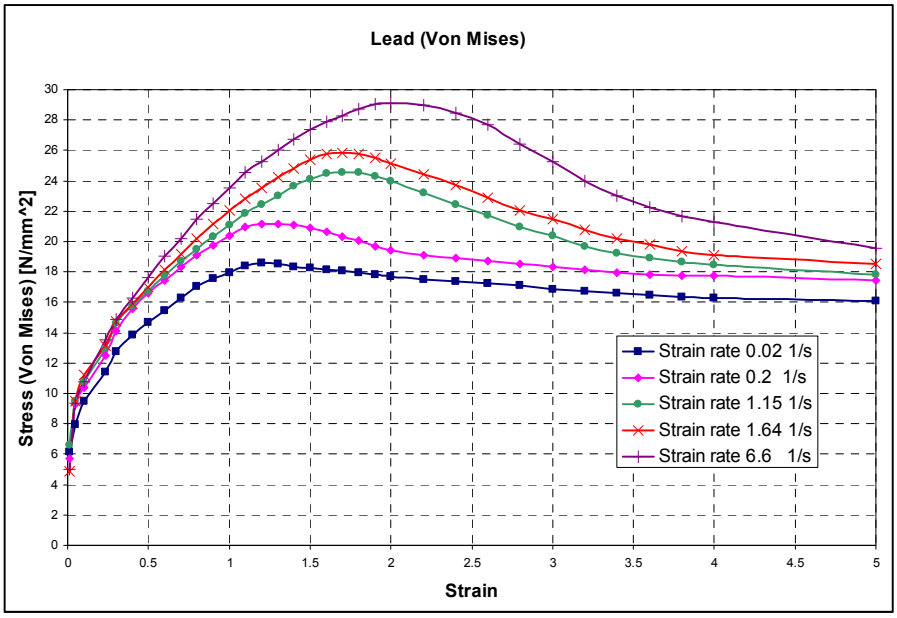

Fig. 4. Stress-strain curves for lead samples tested at different strain rates

Relationship of effective stresses and strains to shear stresses and strains are [21]:

$\bar{\sigma} = \sqrt{3}\tau$ for Von Mises theory;

$\bar{\varepsilon} = \frac{2}{3\gamma}$

In order to determine the deformation flow patterns, square grids of 2mm x 2mm were scriben on the plane of one of the two matching halves of the initial specimens. The two halves were cemented together and then extruded to the desired dimensions. After extrusion the solid halves were removed and splitted to reveal the deformation flow patterns as it can be seen in figure 5[14].

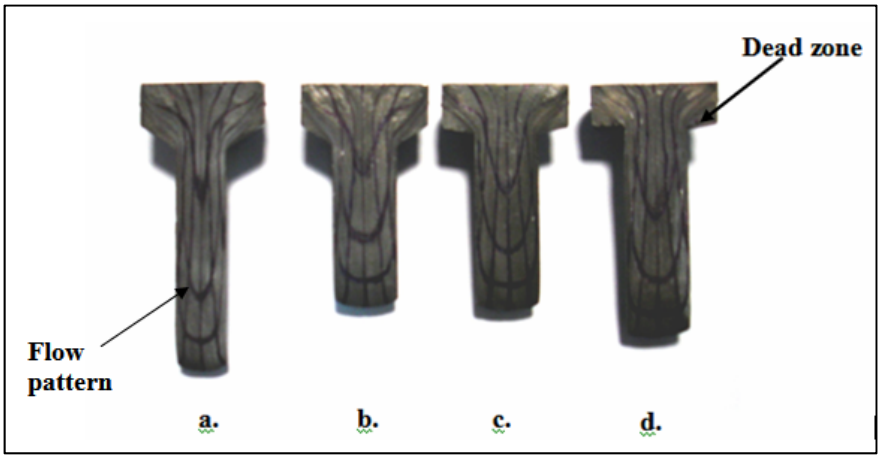

Fig. 5. Deformation flow pattern for different die angle a. 60^0; b. 70^0; c. 80^0; d. 90^0

A numerical simulation of the extrusion process was performed using the finite element software. The two dimensional CAD model was meshed and material properties and boundary conditions were added. In order to determine the deformation parameters (effective stress and strain) in finite element analysis were used the values from flow curve (Fig.4).

The geometries of the billet, die, container and ram were generated in SolidWorks and the meshes within their space domains in MSC SuperForm. The billet was considered thermo-viscoplastic while the tools rigid, and both of these material models neglected the elastic deformation. The shear-type friction conditions at the workpiece and tooling interfaces were imposed as part of the boundary conditions. The friction factor, according to Tresca friction law, at the billet–container and billet–die interfaces were assumed to be 0,3. Extrusion force, effective stress, strain and material flow patterns are presented in figures 6 and 7 for different process conditions. The magnitude of the extrusion forces obtained from the FE simulation were compared to experimental values.

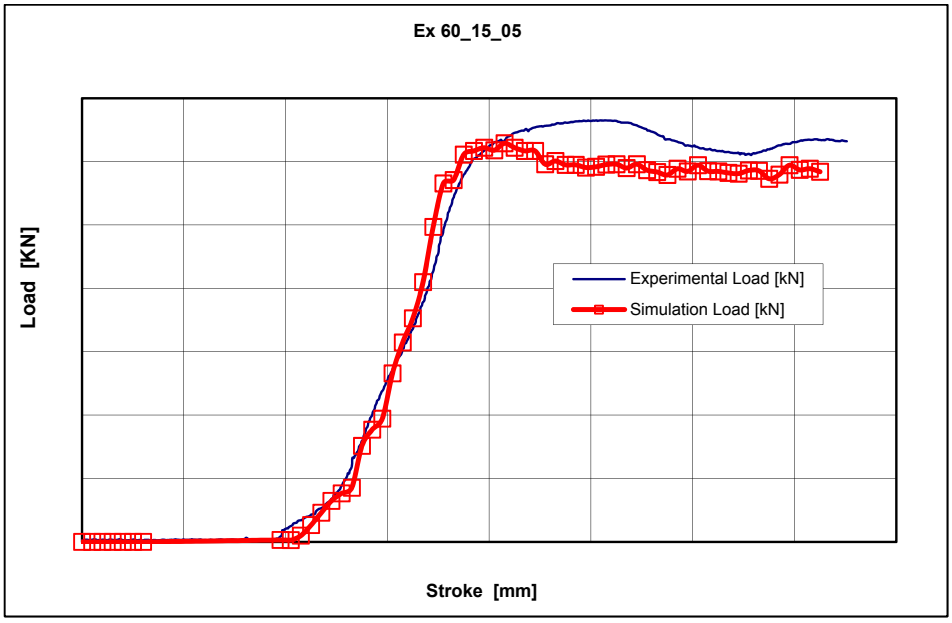
Ex 60_15_05
Load [KN]
Stroke [mm]
Experimental Load [kN]
Simulation Load [kN]

a.

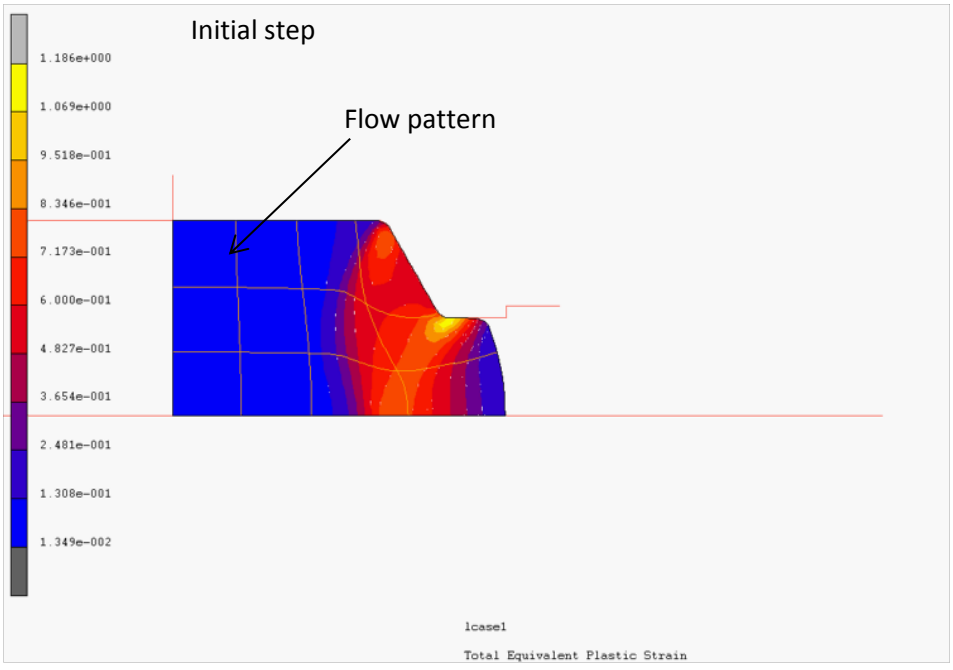
Initial step
Flow pattern
1.186e+000
1.069e+000
9.518e-001
8.346e-001
7.173e-001
6.000e-001
4.827e-001
3.654e-001
2.481e-001
1.308e-001
1.349e-002
lcase1
Total Equivalent Plastic Strain

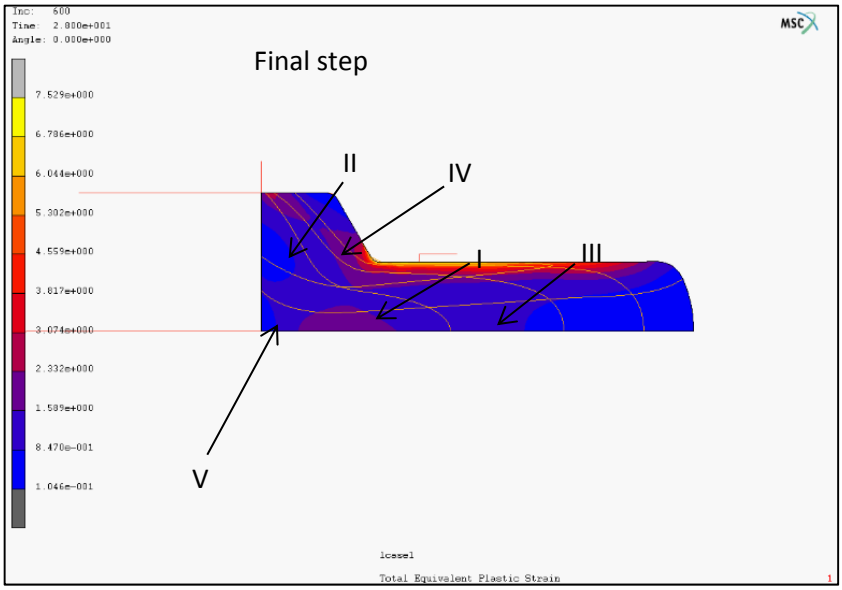

b.

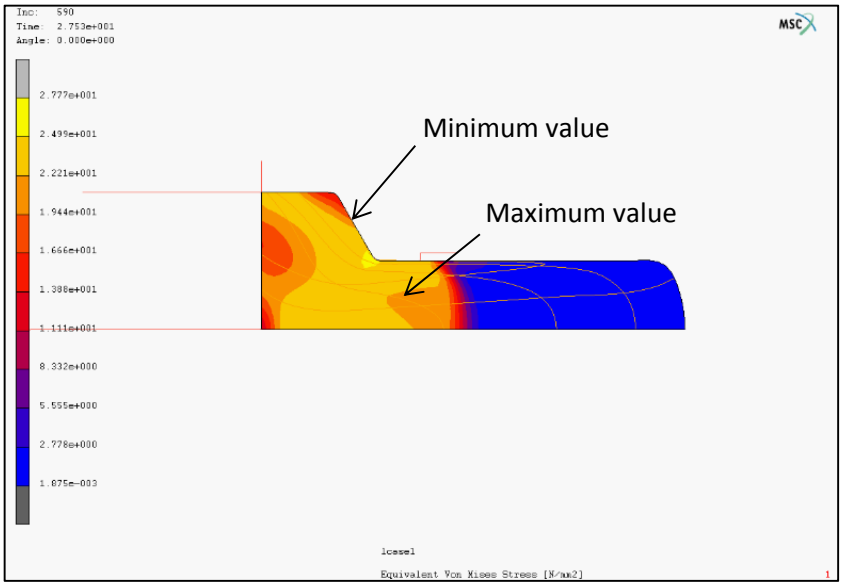

c.

a. extrusion force; b. equivalent strain; c. equivalent von Mises stress
I-primary deformation zone; II-secondary deformation zone;
III-shear zone; IV-primary dead zone; V- secondary dead zone

Fig. 6. Distribution of process parameters for die angle 60^0,
area reduction 17%, ram speed 5mm/s

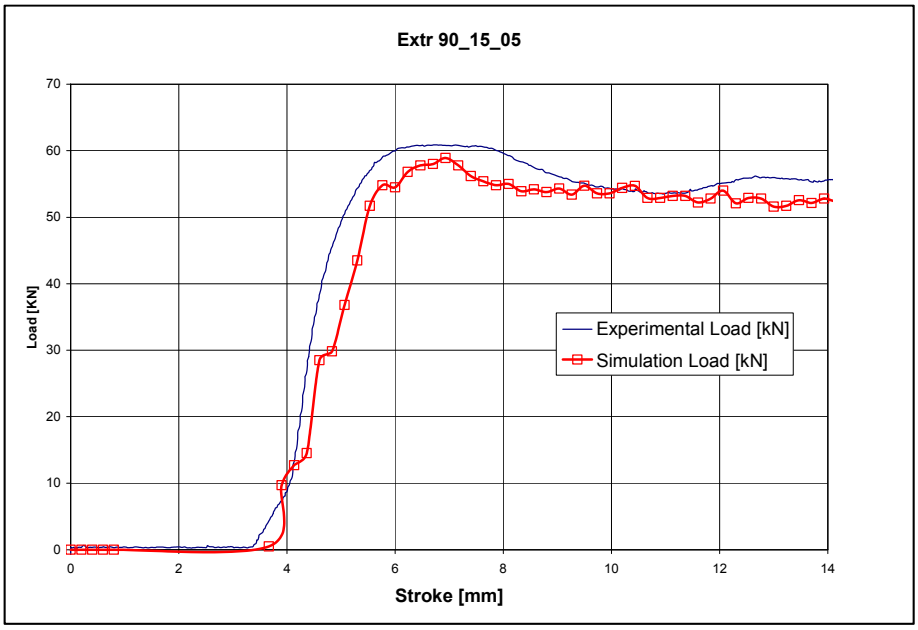
Extr 90_15_05
Load [KN]
Stroke [mm]
Experimental Load [kN]
Simulation Load [kN]
0
10
20
30
40
50
60
70
0
2
4
6
8
10
12
14

a.

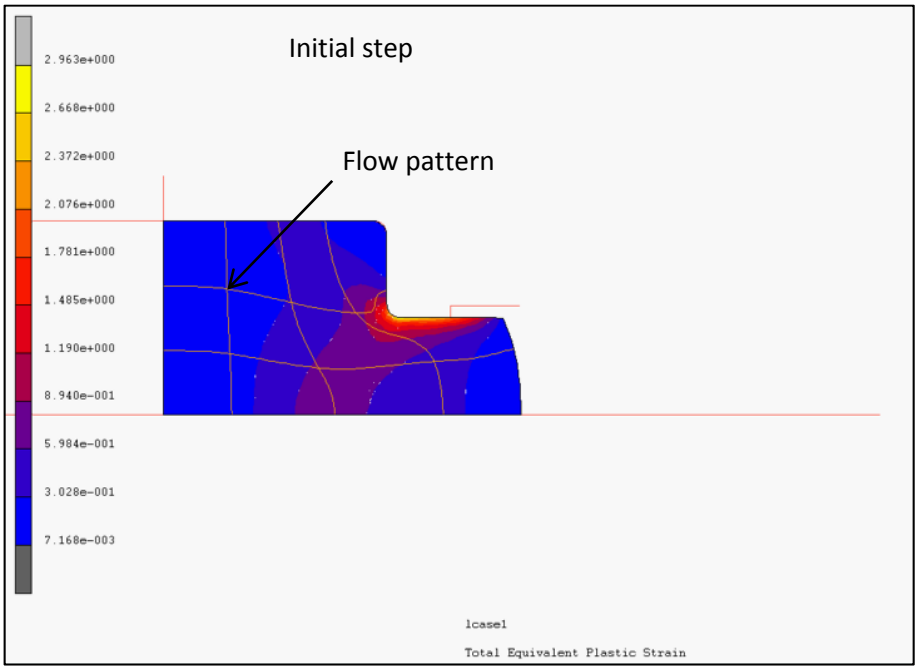
Initial step
Flow pattern
2.963e+000
2.668e+000
2.372e+000
2.076e+000
1.781e+000
1.485e+000
1.190e+000
8.940e-001
5.984e-001
3.028e-001
7.168e-003
lcase1
Total Equivalent Plastic Strain

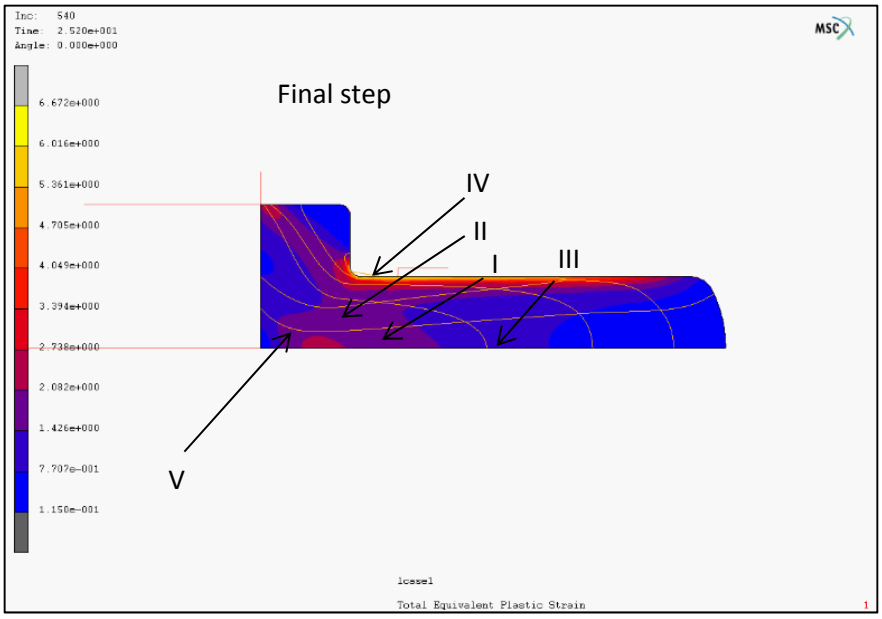

b.

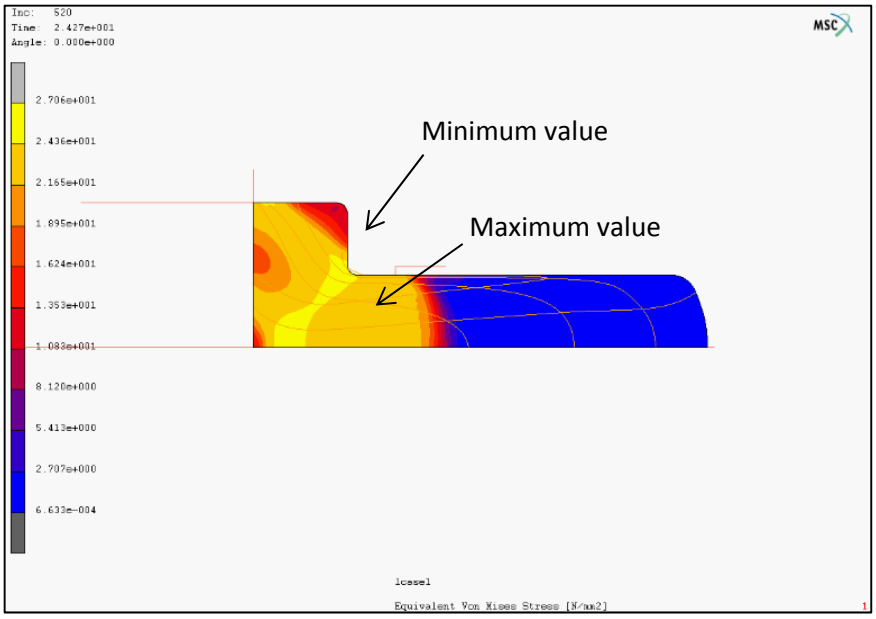

c.

a. extrusion force; b. equivalent strain; c. equivalent von Mises stress

Fig. 7. Distribution of process parameters for die angle 90^0, area reduction 17%, ram speed 5mm/s

Figure 4 shows the true strees – strain curve, named the flow curve that gives the stress required to cause the metal flow plastically. In case of lead alloy the stain rate has an important influence on true stress.

The magnitude of the extrusion force obtained from the FE simulation was compared to experimental values and as is shown in figures 6 and 7 were in good agreement. The maximum level of effective von Mises stresses occurs in the work piece at the exits of the die.

The results indicate that as the die angle is reduced to 60^0, larger extrusion forces are required to extrude lead alloy. This is due to the increased contact length between the die and the work piece leading to high friction power losses.

An important aspect is the temperature inhomogeneity on the cross-section of the workpiece that is more pronounced when ram speed is higher. The thermal effects results in characteristic variation of extrusion load. At a lower ram speed, the decrease of extrusion load is faster during the steady-state extrusion, due to more heat generation (heat generation due to deformation, heat generation due to friction and shear at the billet–die interfaces, heat generation due to friction at the extrudate–die interface), and thus decreased flow stress, as the process proceeds. The material flow pattern is influenced by local friction conditions and die geometric shape. These aspects influenced the size of the dead zone in the material as is shown in figure 5. In these flow patterns of the extruded lead at 90^0 die angle, the boundary of the dead l zone is clearly visible, as zones of intense shear. Due to friction forces between work piece and die and, the material on the inside tends to move faster than the outside.

For a die angle of 90 °, nonuniform material flow due to high friction. By reducing the die angle to 60^0 the deformation in the section is more uniform.

In Figures 6 and 7 the distribution of strain and stress in proximity of the final deformation stroke are respectively plotted: five different zones can be evidenced depending on the amount of strain. In the billet, the zone IV (primary dead metal zone) is characterized by strains lower than 1, material is highly hydrostatic compressed; in the zone III (intensive shear zone) an high strain is evidenced (5–7); in the zone I (main deformation zone) the material has low strains (below 2,5). In the middle of the billet, behind the primary deformation zone, plastic deformation is much smaller (secondary deformation zone). The metal of the secondary deformation zone gradually flows into the primary deformation zone.

CONCLUSIONS

A successful experimental programme of cold extrusion of lead alloy was carried out. Material flow curve and extrusion forces for different process parameters were determined. The finite element results show good correlation with experimental ones, confirming the accuracy of the finite element model.

Because of sticking friction between billet and container wall the surface layers of the billet will be retained against the container wall. The core of the billet is pushed forward by the advancing ram, and a shear zone forms between the core material, which flows forward, and the peripheral surface layer of the billet, which sticks to the container wall. In the primary dead zone, the billet material located in the corner region between the die and the container wall is situated off from the main stream flowing through the die orifice, and is therefore subjected only to minor plastic deformations. As is can be seen in figure 8 and 9 here small plastic deformations do occur .

The process parameters including die geometry and ram speed has an important influence on material flow during the deformation. The material flow affects the product quality (structure and properties) and the extrusion load.

REFERENCES

[1]. M. SCHIKORRA, L. DONATI, L. TOMESANI, A.E. TEKKAYA, *Microstructure analysis of aluminum extrusion: Prediction of microstructure on AA6060 alloy*, J. Mater. Proc. Tech. 201, pp.156–162, 2008.

[2]. X. MA, M.B.DEROOIJ, D.J.SCHIPPER, *Modelling of contact and friction in aluminium extrusion* , Tribology International 43 , pp.1138–1144, 2010.

[3]. J.S. AJIBOYE, M.B. ADEYEMI, *Effects of die land on the cold extrusion of lead alloy,* Journal of Materials Processing Technology 171, pp. 428–436, 2006.

[4]. S.O. ONUH, M. EKOJA, M.B. ADEYEMI, *Effects of die geometry and extrusion speed on the cold extrusion of aluminium and lead alloys*, J. Mater. Proc. Tech. 132, pp. 274–285, 2002.

[5]. P. TIERNAN, M.T. HILLERY, B. DRAGANESCU, M. GHEORGHE, *Modelling of cold extrusion with experimental verification*, Journal of Materials Processing Technology 168, pp. 360–366, 2005.

[6]. N. SOLOMON, I. SOLOMON, *Effect of die shape on the metal flow pattern during direct extrusion process*, Revista de Metalurgia 46, pp.396-404, 2010.

[7]. DYI-CHENG CHEN, SHENG-KAI SYU, CING-HONG WU, SIN-KAI LIN, *Investigation into cold extrusion of aluminum billets using three-dimensional finite element method*, Journal of Materials Processing Technology 192–193, pp.188–193, 2007.

[8]. L. LI, J. ZHOU, J. DUSZCZYK, *Prediction of temperature evolution during the extrusion of 7075 aluminium alloy at various ram speeds by means of 3D FEM simulation*, Journal of Materials Processing Technology 145, pp. 360–370, 2004.

[9]. I. DRAGAN, *Tehnology of Plastic Deformation*, EDP, Bucharest, Romania, 1981.

[10]. J.-L. CHENOT, E. MASSONI, *Finite element modelling and control of new metal forming processes*, International J. Machine Tools & Manufacture 46 (2006) p. 1194–1200.
[11]. P. HARTLEY, I. PILLINGER, *Numerical simulation of the forging process*, Comput. Methods Appl. Mech. Engrg. 195 (2006) p. 6676–6690.
[12]. JI HYUN SUNG, JI HOON KIM, R.H. WAGONER ,*A plastic constitutive equation incorporating strain, strain-rate and temperature,* International Journal of Plasticity 26 (2010) 1746–1771.
[13]. Y. LEE, B.M. KIM, K.J. PARK, S.W. SEO, O. MIN, *A study for the constitutive equation of carbon steel subjected to large strains, high temperatures and high strain rates,* Journal of Materials Processing Technology 130–131 (2002) 181–188.
[14]. M.POP, s.a., Experimental and numerical aspects regarding lead alloy plastic deformation, Revue Roumaine des Sciences Techniques Série de Mécanique Appliquée, Tome 57, No 1, 2012, pp71-85.
[15]. M. POURSINAA, H. EBRAHIMIB, J. PARVIZIANC, *Flow stress behavior of two stainless steels, An experimental–numerical investigation*, J. Mater. Process. Technol. 199(2008) p. 287–294.
[16]. R.G. SNAPE, S.E. CLIFT, A.N. BRAMLEY, *Sensitivity of finite element analysis of forging to input parameters,* Journal of Materials Processing Technology 82 (1998) 21–26.
[17]. H.S. VALBERG, *Applied Metal Forming Including FEM Analysis*, Cambridge University Press, 2010.
[18]. H. NANHAI, L. KEZHI, *Numerical design of the die land for shape extrusion,* J. Mater. Proc. Tech. 101, pp.81–84, 2000.
[19]. HEINZ TSCHAETSCH, *Metal Forming Practise, Processes – Machines – Tools*, Springer, 2006.
[20]. K.LAUE, H. STENGER, *Extrusion*, American Society for Metals, 1981.
[21]. METALS HANDBOOK, Vol.8, *Mechanical testing*, ASM International, 1990.

STUDIA UBB PHYSICA, Vol. 58 (LVIII), 2, 2013, pp. 67-74
(RECOMMENDED CITATION)

HIGH FIELD MRI INVESTIGATION OF EYE STRUCTURES AFTER UV-B IRRADIATION

E. VANEA[a], C. MORARU[a], S. MUREŞAN[b], R. MOLDOVAN[b], A. FILIP[b], A. MUREŞAN[b], S. SIMON[a,*]

ABSTRACT. High-field Magnetic Resonance Imaging (MRI) has been employed in this study to reveal *in vivo* the structures of the eyes in relation to other parts of the head before and after ultraviolet irradiation. No anatomical changes or major injuries have been identified in the eyeball post irradiation with UV-B radiation of 360 mJ/cm^2, for 5 min, but the high resolution MRI images recorded with the 7 T MRI system, without making use of any contrast agent, are strongly supporting the use of high field MRI system in ophthalmology.

Keywords: MRI; UV-B radiation; eye irradiation.

INTRODUCTION

Ophthalmology offers today several optical techniques for eyes imaging in clinical setting [1]. Although these procedures lead to high resolution information, they have limitations as diagnostic and prognostic tools when an eye internal function is concerned. Magnetic resonance imaging (MRI) has been developed for imaging of different parts of the body, to provide clinically relevant information, especially where the desired information is difficult to be obtained by other techniques. MRI uses non-ionizing radiation and has the capability of imaging, with a superior soft tissue contrast, thin slices of tissue in any orientation and depth with submillimeter resolution. Numerous strategies for ocular MRI have been attempted over the years. MRI techniques allow to clarify difficult ocular diagnoses and to assess the disease mechanisms and the effect of therapies. In general, high-resolution MRI technique provides in a noninvasive manner detailed images

[a] *Babes-Bolyai University, Faculty of Physics & Institute of Interdisciplinary Research in Bio-Nano-Sciences, Cluj-Napoca, Romania, * Corresponding author: simion.simon@phys.ubbcluj.ro*
[b] *Iuliu Haţieganu University of Medicine and Pharmacy, Department of Physiology, Cluj-Napoca, Romania*

of the eye anatomy including retina/choroid complex (total thickness) and optic nerve head [2]. MRI with better resolution is expected as clinical MRI system move from the 1.5 T devices to 3 or even 7 T, providing better resolution at higher speeds, resulting in less motion artefacts [1].

MRI scans focused on the orbits may be acquired performing a cranial scan by mean of a whole-body coil or a head coil [3, 4]. These coils provide orbital images in the context of the head, as the signal penetrates beyond the orbital apex [3]. The surface coil (~ 5 cm inner diameter) can be used to image the eye selectively, providing a good resolution of the structures within the eye [5, 6]. However surface coil techniques, can be much more sensitive to movement artefacts [1].

The eye is an organ anatomically distinct with structures that requires high spatial resolution to be visualized. MRI contrast between different eye structures can be obtained based on the differences in their water content and mobility. The human aqueous humor is a clear liquid having properties similar to that of water, while the vitreous humor is an avascular jelly containing 98% water [7].

Ultraviolet-B (UV-B 280–320 nm) and ultraviolet-A (UV-A 320–400 nm) are essential components of sunlight that may induces damages in biological systems [8, 9]. Irradiation by UV light is one of the most common causes of eye injuries. Ocular injuries induced by UV light can occur through either a photooxidation reaction or an inflammatory response. Photooxidation reactions are driven by absorbing light of sensitizing compounds in the eye and can produce reactive oxygen species and free radicals [10].

These reactive oxygen species and free radicals are involved in lipid peroxidation and protein damage. The eye structures most damaged by UV radiation are mainly cornea, uvea (iris, ciliary body, choroid), lens and retina. Diseases of cornea associated with UV irradiation are photokeratitis, pingueculae and pterygia. The most common malignant tumor of the eye is uveal melanoma, and has UV light as a factor in its etiology. Lens are affected by UV light, because protein fibers that are in its composition are affected by free radicals and in time its loses their transparency and cause cataracts. Deterioration of the macula (central) cells in the retina can be caused also by UV radiation (macula degeneration) [11, 12].

In the present study MRI experiments were conducted by means of a 7 T system on laboratory rats in order to reveal possible changes induced in ocular structures that might occur as a result of the ultraviolet irradiation.

MATERIALS AND METHODS

The MRI experiments were carried out before and 24 hours post UV-B irradiation. Two male adult rats, Wistar type (120-200 g), were exposed to UV-B

radiations for 5 min (360 mJ/cm^2 UV-B). The animals were anesthetized intra-peritoneally with a 4:1 ketamine:xylazine mixture (100 mg/kg: 25 mg/kg body weight), respectively. Rectal temperature was continuously monitored and maintained within normal physiological limits. MRI investigations were performed with a Bruker BioSpin MRI equipment PharmaScan of 7.0 Tesla magnet. Rat head was fixed using a special device placed in a head volume coil 1 H RES 300 075/040 TR QSN. Anatomical images (using the Tripilot protocol) were initially obtained in order to allow the correct positioning of the animal inside the coil. T2 weighted RARE (rapid acquisition with relaxation enhancement) MRI images were acquired in coronal section allows simultaneous viewing of both ocular lobes. The imaging parameters used were FOV (field of view) = 4 cm x 4 cm, matrix = 256 x 256, slice thickness = 1 mm, number of slices = 5; repetition time (TR) = 33 ms, time to echo (TE) = 2303.34 ms. The time for each scan was ~ 9 min. Images were processed using Onis 2.4 software.

RESULTS AND DISCUSSION

MRI images obtained for the two rats, noted I and II, before and 24 hours post UV-B irradiation are presented in Figure 1.

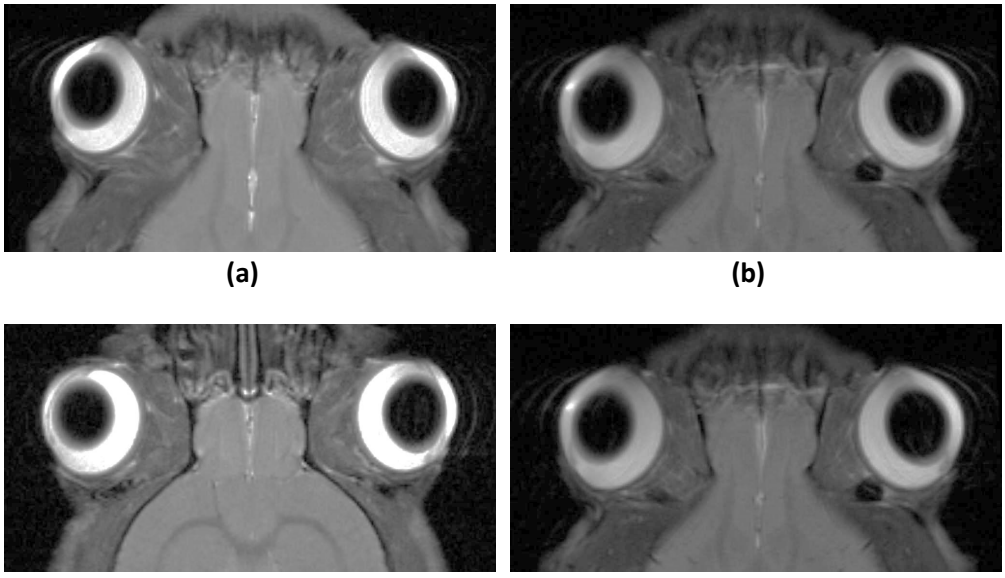

Fig. 1. T2 weighted coronal MRI images recorded from rat I **(a)** before and **(b)** after exposure to UV radiation; and rat II **(c)** before and **(d)** after exposure to UV radiation.

The post irradiation MRI images reveal no anatomical structure changes or major injuries that could have been induced to the eyeball in the first 24 hours post irradiation. Neural tissue visualization is a substantial advantage of MRI over any other ocular imaging technique because allows visualization of the cranial and intraorbital structures and identification of the etiology of ocular abnormalities [1, 13].

As can be seen in Figure 2, the penetration and absorption of UV light in the eye varies by wavelength and depend on the tissue upon which it is incident. A longer wavelength cause a deeper penetration of the radiation through the structures of the eye. Cornea can potentially be affected by all wavelengths of UV light, while retina, the most deeper tissue of the eye, can be affected by longer wavelengths of UV light [14]. That is why UV-B light should not affect very much the posterior part of the eye (1% absorption of UV-B light at the vitreous level).

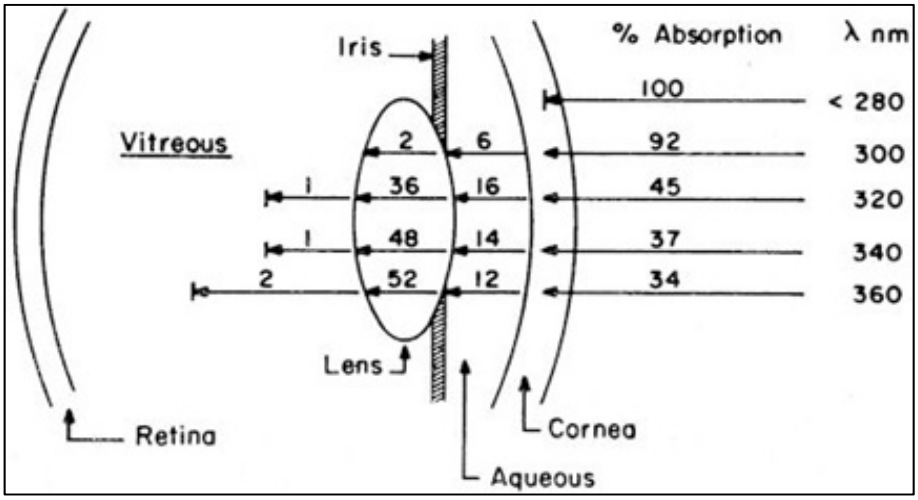

Fig. 2. UV penetrance in the human eye [14].

It is worth pointing out that rats eye anatomy differs from that of human eye. The eyes of rats are small but they have an enormous depth of focus [15].The lens is larger within the eye in comparison with the lens of the human eye (see Figure 3). UV radiation can penetrate deeper, closer to retina and maybe can determine more damages to the posterior eye structure.

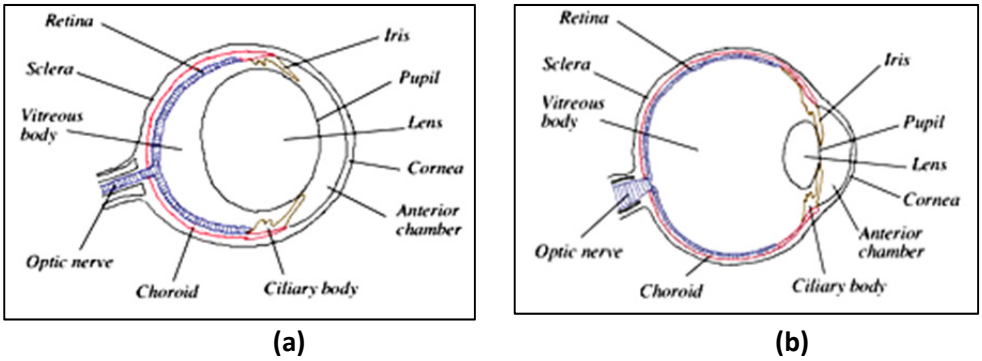

Fig. 3. Anatomical drawing at different scales of (a) rat eye (adapted from [16]), and (b) human eye [17].

In this case, for the UV irradiated rat eyes a possible inflammation of retina/choroid complex and optic nerve (see Figures 4 and 5) could be considered. Retina/choroid complex thickness and optic nerve with its associated venous plexus within extraocular musculature varies from ~0,34 mm before irradiation to ~0,37 mm after irradiation, and from ~0,88 mm to ~0,90 mm, respectively. On the other hand, possible errors occurring during the measurement process have to be taken into account. Slices are not exactly in the same position before and after irradiation, and the edges of the eye structures are difficult to be precisely evaluated. These irradiation effects must be confirmed also by other investigations. There are other techniques like electrophysiology that can evidence retinal damages [18]. Optic nerve damages can be also observed through optical coherence spectroscopy [19].

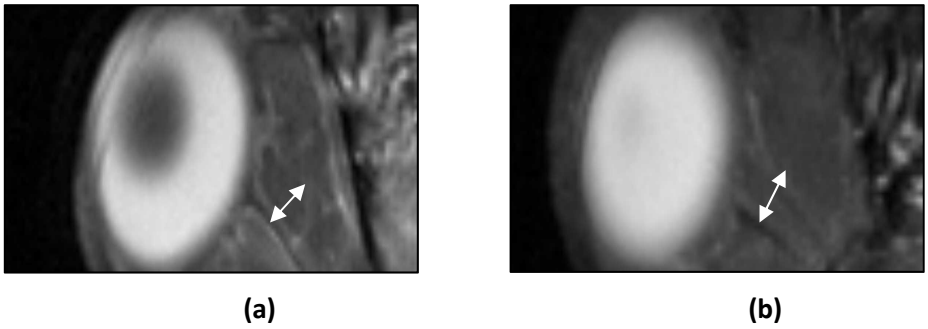

Fig. 4. Selected MRI image of the optic nerve of the rat eye (a) before irradiation and (b) post irradiation.

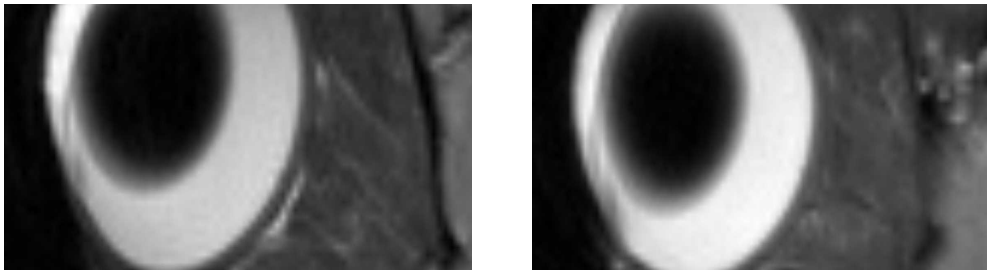

(a) **(b)**

Fig. 5. Selected MRI image of the retina/choroid complex of the rat eye (a) before irradiation and (b) post irradiation.

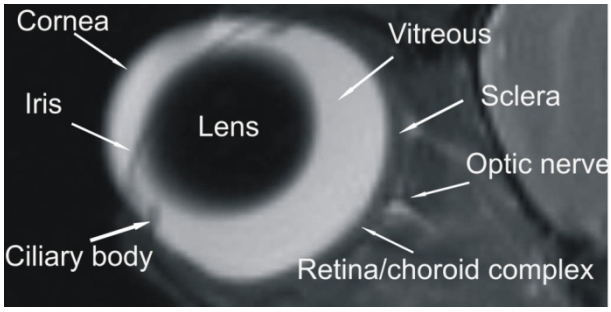

Fig. 6. Selected MRI image of the rat eye. Eye structures such as the lens, iris, ciliary body, vitreous, sclera, retina/choroid complex and the location of the optic nerve head are visualized.

From Figure 6, can be seen, more in detail, that MRI technique can evidence the eye structures such as the lens, cornea, iris, ciliary body, retina/choroid complex, sclera and optic nerve and its associated venous plexus within extraocular musculature.

The 7T high magnetic field strength allows to achieve an enhanced signal-to-noise ratio (SNR) for the MRI images and implicitly a higher spatial resolution. The SNR of the images decreases with a decrease in voxel size, but increases with the magnetic field strength used for MRI image acquisition [7].

CONCLUSIONS

High field resolution 7T MRI techniques are able to provide qualitative information of the eyes inrelation to otherparts of thehead, even without contrast agents, with potential clinical applications in ophthalmology. Because of rat eye anatomy, different from that of human eye, UV-B radiation has potentially strength to damage also the posterior part of the rat eyes, so 7T MRI system can be used to study damages on optic nerve level.

REFERENCES

[1]. K.A. Townsend, G. Wollstein, J.S. Schuman, Clinical application of MRI in ophthalmology, *NMR Biomed.* (2008) 21, 997–1002.
[2]. H. Luan, R. Roberts, M. Sniegowski, D.J. Goebel, B.A. Berkowitz, Retinal thickness and subnormal retinal oxygenation response in experimental diabetic retinopathy, *Invest. Ophtha. Vis. Sci*. (2006) 47, 320-328.
[3]. J.D Wirtschafter, E.L. Berman, C.S. McDonald, Magnetic resonance imaging and computed tomography: Clinical neuro-orbitall anatomy. American Academy of Ophthalmology, San Francisco, 1992.
[4]. J.F. Schenck, W. Leue, Instrumentation: Magnets, coils, and hardware, in: S. Atlas (Ed.) *Magnetic Imaging of the Brain and Spine*, Raven Press, New York, 1991.
[5]. R.J. Bert, S. Patz, M. Ossiani, S.D. Caruthers, H. Jara, J. Krejza, T. Freddo, High-resolution MR imaging of the human eye 2005, *Acad. Radiol*. (2006) 13, 368–378.
[6]. T. Georgouli, T. James, S. Tanner, D. Shelley, M. Nelson, B. Chang, O. Backhouse, D. McGonagle, High-resolution microscopy coil MR-eye, *Eye* (2007) 22, 994-996.
[7]. L. Fanea, A.J. Fagan, Review: Magnetic resonance imaging techniques in ophthalmology, *Mol. Vis*. (2012) 18, 2538-2560.
[8]. J. Wenk, P. Brenneisen, C. Meewes, M. Wlaschek, T. Peters, R. Blaudschun, W. Ma, L. Kuhr, L. Schneider, K. Scharffetter-Kochanek, UV-induced oxidative stress and photoaging, *Curr. Probl. Dermatol*. (2001) 29, 83–94.
[9]. R.S. Klein, V.P. Werth, J.C. Dowdy, R.M. Sayre, Analysis of compact fluorescent lights for use by patients with photosensitive conditions, *Photochem. Photobiol*. (2009) 85, 1004–1010.
[10]. A.R. Wielgus, J.E. Roberts, Retinal photodamage by endogenous and xenobiotic agents, *Photochem.Photobiol*. (2012) 88, 1320-1345.
[11]. J.G.M. van KuijkFrederik, Effects of ultraviolet light on the eye: role of protective glasses. *Environ.Health Persp*. (1991) 96, 177-184.
[12]. J.E. Roberts,Ocular phototoxicity, *J. Photoch. Photobio. B*, (2001) 64, 136–143.

[13]. J.M. O'Brien, Retinoblastoma: clinical presentation and the role of neuroimaging, *Am. J. Neuroradiol*. (2001) 22, 426–428.
[14]. G.J. Johnson, The environment and the eye, *Eye* (2004) 18, 1235–1250.
[15]. D.G. Green, M.K. Powers, M.S. Banks, Depth of focus, eye size and visual acuity, *Vision Res*. (1980) 20, 827-835.
[16]. W.E. Fry, The eye of the albino rat. In: The rat in laboratory investigation. E. J. Farris and J. Q. Griffith, eds. 2nd edn, Philadelphia, J.B. Lippincott Comp., 1949.
[17]. http://www.ratbehavior.org
[18]. H. Ikeda, E. Adachi-Usami, M. Saeki, N. Takeda, T. Kimura, Electrophysiological studies on light damage in the mouse retina after sodium iodate injection, *Ophthalmologica*, (1994) 208, 220-225.
[19]. L.M. Sakata, J. Deleon-Ortega, V. Sakata, C.A. Girkin, Optical coherence tomography of the retina and optic nerve - A review, *Clin. Exp. Ophthalmol*. (2009) 37, 90-99.

STUDIA UBB PHYSICA, Vol. 58 (LVIII), 2, 2013, pp. 75-81
(RECOMMENDED CITATION)

XPS AND XRD INVESTIGATION OF IRON DOPED NANOCRYSTALLINE HYDROXYAPATITE

B. OPREA[a], C. MIRESTEAN[a], G. DINDELEGAN[b], S. SIMON[a,*]

ABSTRACT. This paper reports on some properties of pure and iron doped samples of hydroxyapatite composition prepared by coprecipitation method. The samples were characterized by X-ray photoelectron spectroscopy (XPS) and powder X-ray diffraction (XRD). The XPS results show on surface of both undoped and iron doped samples a Ca/P atomic ratio close to 1.67 typical for hydroxyapatite. According to XRD results, the addition of 0.1 wt % Fe_2O_3 promotes in the sample of pure hydroxyapatite composition the growth of nanocrystalline hydroxyapatite.

Keywords: *hydroxyapatite, iron doping, XPS, XRD.*

INTRODUCTION

Hydroxyapatite, $Ca_{10}(PO_4)_6(OH)_2$, is the major inorganic component of bone and owns high biocompatibility with the tissues. Hydroxyapatite has become the most common material to replace bone or to guide its regeneration, currently used in orthopedic and dental implants. Synthetic hydroxyapatite for medical use as implant material resembles in its chemical composition the natural bone mineral. The porosity, impurities and the size of the crystallites influence degradation behaviour *in vitro* but not the binding of bone tissue [1]. The dimension of hydroxyapatite crystals seems to determine the mechanisms of active resorption, and nanocrystalline hydroxyapatite should have the potential to show a better resorbability [2]. At the same time, the surface properties of a biomaterial play a significant role in the cell response. X-ray photoelectron spectroscopy is an important surface analytical tool used to examine the surface of biomaterials based on hydroxyapatite [3-5].

[a] *Babes-Bolyai University, Faculty of Physics & Institute of Interdisciplinary Research in Bio-Nano-Sciences, 400084 Cluj-Napoca, Romania, * Corresponding author: simion.simon@phys.ubbcluj.ro*

[b] *Iuliu Hatieganu University of Medicine and Pharmacy, Faculty of Medicine, 400012 Cluj-Napoca, Romania*

The aim of the study was to investigate by X-ray diffraction (XRD) and X-ray photoelectron spectroscopy (XPS) pure and iron doped samples of hydroxyapatite composition prepared by coprecipitation method.

EXPERIMENTAL

Samples of pure hydroxyapatite composition, $Ca_{10}(PO_4)_6(OH)_2$, and doped with iron (0.1 wt%) were prepared with a Ca/P ratio in precursors of 1.67, from a $Ca(NO_3)_2$ solution (0.2 M) which was added added droplet by droplet, during three hours, to a $(NH_4)_2HPO_4$ aqueous solution (0.2 M) under constant stirring at 90°C. For iron doping was used a $Fe(NO_3)_3$ aqueous solution (0.2 M). Thereafter the precipitates were filtrated, washed with deionized water and dried in air under normal pressure at 110° C for 24 hours. A part of the samples was heat treated at 300 ^oC for 30 minutes.

The composition on the surface of the samples was analysed using the survey XPS spectra recorded on a SPECS PHOIBOS 150 MCD equipment, with a monochromatic Al K_α (hν=1486.6 eV) X-ray source (260 W). The pressure in the analysis chamber was about 5x 10^{-10} mbar. A flood-gun was used in order to neutralize the electrostatic charge on the surface of the samples. The XPS spectra were referenced with respect to the C 1s peak at 284.6 eV originating from carbon contamination. Data analysis was done using the Casa XPS software [6]. The structure of the samples was analysed on a Shimadzu XRD 6000 X-ray diffractometer, using CuKα radiation (λ = 1.5418Å). The operation voltage and current were 40 kV and 30 mA. The crystallites size has been estimated by Scherrer formula [7].

RESULTS AND DISCUSSION

The analysis of the XPS survey spectra recorded from the samples of pure hydroxyapatite composition (Fig. 1) as well as that recorded from iron doped (0.1 wt% Fe_2O_3) samples (Fig. 2) point out an atomic Ca/P ratio close to 1.6, in agreement with the expected composition according to the precursor amounts introduced in the solutions used for the samples synthesis by coprecipitation. The presence of iron is evidenced by the weak photoelectron signals occurring at 720 eV and 707 eV from Fe $2p_{1/2}$ and Fe $2p_{3/2}$ spin-orbit splitting of iron spectral line (Fig. 3). The 300 ^oC treatment leads to a slightly enhanced iron content on the surface of the iron doped sample.

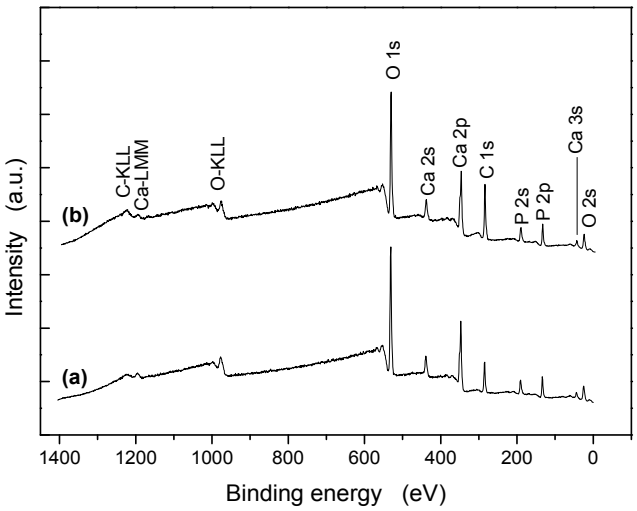

Fig. 1. XPS survey spectra recorded from (a) as prepared, and (b) 300 ^{o}C treated samples of pure hydroxyapatite composition.

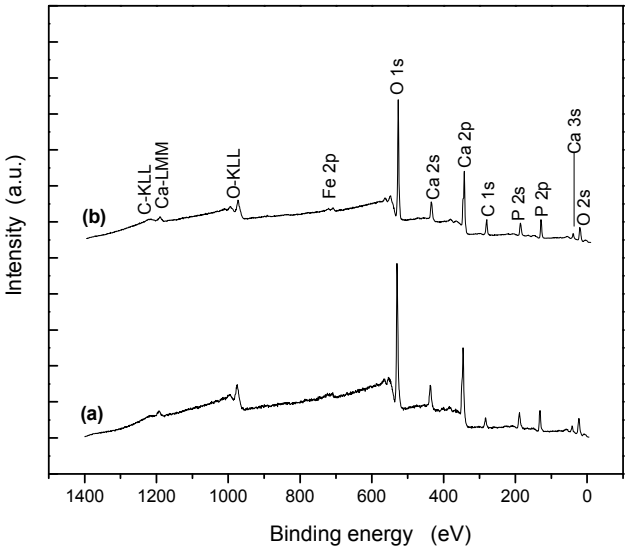

Fig. 2. XPS survey spectra recorded from (a) as prepared, and (b) 300 ^{o}C treated samples of iron doped hydroxyapatite.

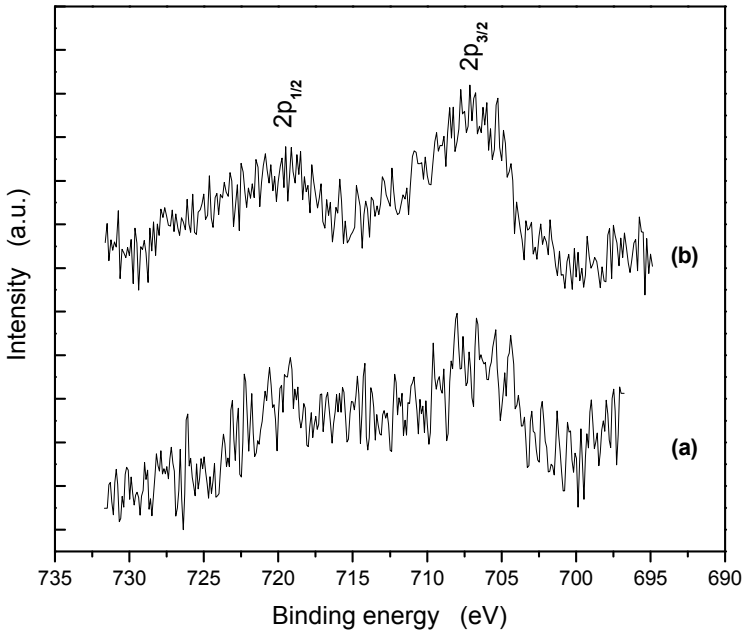

Fig. 3. Fe 2p core level photoelectron spectra recorded from (a) as prepared, and (b) 300 ^{o}C treated samples of iron doped hydroxyapatite.

Further XRD analysis on the structure of the samples shows that in the samples of pure hydroxyapatite composition (Fig. 4) a nanocrystalline phase of monetite type (*JCPDS-PDF* 071-1760) is developed. In monetite, of $CaHPO_4$ composition, the Ca/P ratio is 1, while the XPS results indicate a higher Ca/P ratio, closer to hydroxyapatite composition, that could be due to a dominant hydroxyapatite phase in disordered structural state, without signature in the XRD patterns. The X-ray diffraction results are different for the iron doped samples (Fig. 5), wherin the 0.1 wt% Fe_2O_3 addition promotes the development of nanocrystalline hydroxyapatite phase (JCPDS-PDF *74-0565*). This demonstrates that a very low content of iron can change the structure of calcium phosphate compound of pure hydroxyapatite composition from nanocrystalline monetite to nanocrystalline hydroxyapatite.

The size of monetite crystallites estimated by Scherrer formula is about 100 nm (Fig. 4), and that of hydroxyapatite crystallites in iron doped samples is about 20 nm (Fig. 5).

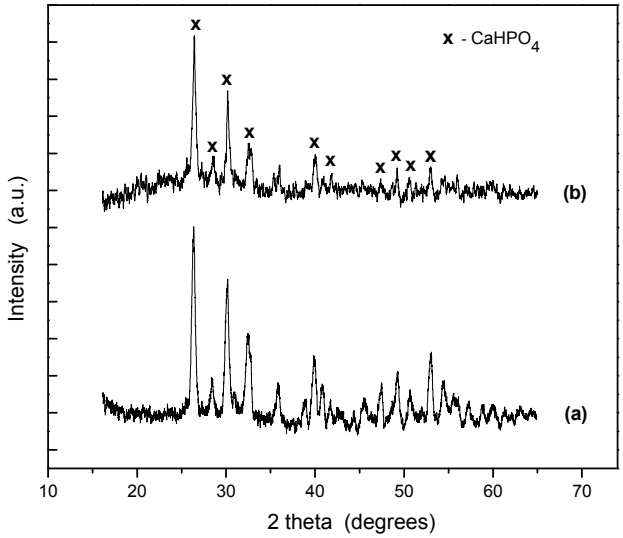

Fig. 4. XRD patterns recorded from (a) as prepared, and (b) 300 ^{o}C treated samples of pure hydroxyapatite composition.

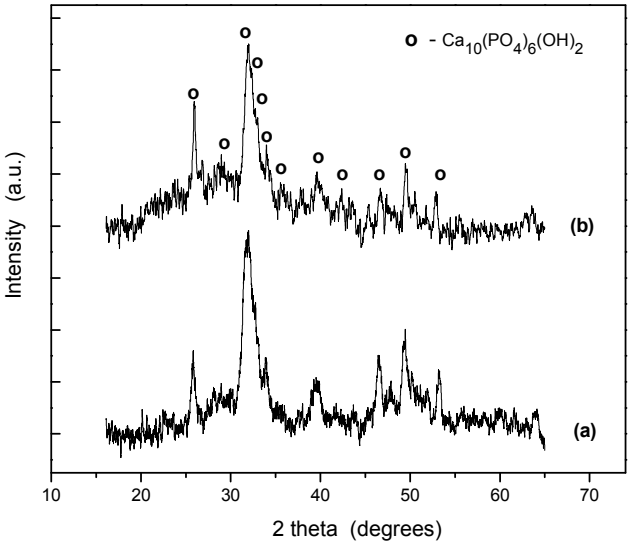

Fig. 5. XRD patterns recorded from (a) as prepared, and (b) 300 ^{o}C treated samples of iron doped hydroxyapatite.

As already reported, the impurities in synthetic hydroxyapatite used for biomedical applications do not affect the binding of bone tissue [1]. On the other hand, the iron doped hydroxyapatite is considered for the hyperthermia treatment of bone tumors in form of permanent implants [8-12]. At the same time, a higher bioactivity is expected from the nanocrystalline samples than from that with large sized crystals [5, 13-16]. In the samples we investigated, the crystallite sizes could confer beside a good bioactivity also the potential for a better resorbability.

CONCLUSIONS

Pure and iron doped samples of hydroxyapatite composition prepared by coprecipitation method have on surface a Ca/P atomic ratio close to 1.67 typical for hydroxyapatite. A slightly enhanced iron content on the surface of the iron doped sample is induced after 30 minutes treatment at 300 ^{o}C.

In the the samples of pure hydroxyapatite composition a nanocrystalline phase of monetite type is developed that is assumed to occur beside a dominant hydroxyapatite phase in disordered structural state. The doping with 0.1 wt% Fe_2O_3 promotes the development of nanocrystalline hydroxyapatite phase and demonstrates that a very low content of iron can change the the structure of calcium phoshate compound of pure hydroxyapatite composition from nanocrystalline monetite to nanocrystalline hydroxyapatite.

ACKNOWLEDGEMENTS

This research was accomplished in framework of PN-II PCCA-78/2012 project granted by UEFISCDI – Romania.

REFERENCES

[1]. P.S. Eggli, W. Muller, R.K. Schenk, Porous hydroxyapatite and tricalcium phosphate cylinders with two different pore size ranges implanted in the cancellous bone of rabbits. A comparative histomorphometric and histologic study of bone ingrowth and implant substitution, *Clin. Orthop. Relat. Res*. (1988) 232, 127–138.

[2]. J. Brandt, S. Henning, G. Michler, W. Hein, A. Bernstein, M. Schulz, Nanocrystalline hydroxyapatite for bone repair: an animal study, *J. Mater. Sci. Mater. Med*. (2010) 21, 283–294

[3]. G.N. Raikar, J.L. Ong, L.C. Lucas, Hydroxyapatite characterized by XPS, *Surf. Sci. Spectra* (1996) 4, 9–13.
[4]. H.B. Lu, C.T. Campbell, D.J. Graham, B.D. Ratner, Surface characterization of hydroxyapatite and related calcium phosphates by XPS and TOF-SIMS, *Anal. Chem.* (2000) 72, 2886–2894.
[5]. V. Simon, D. Lazar, R.V.F. Turcu, H. Mocuta, K. Magyari, M. Prinz, M. Neumann, S. Simon, Atomic environment in sol-gel derived nanocrystalline hydroxyapatite, *Mater. Sci. Eng. B Adv*. (2009) 165, 247–251.
[6]. N. Fairley, A. Carrick, The Casa Cookbook – Part I: Recipes for XPS data Processing; Acolyte Science: Knutsford, Cheshire 2005.
[7]. A.L. Patterson, The Scherrer formula for X-ray particle size determination**,** *Phys. Rev*. (1939) 56, 978-982
[8]. K.A. Gross, R. Jackson, J. D. Cashion, L. M. Rodriguez-Lorenzo, Iron substituted apatites: A resorbable biomaterial with potential magnetic properties, *Eur. Cells Mater*. (2002) 3 (S2) 114–117.
[9]. D. Eniu, D. Cacaina, M. Coldea, M. Valeanu, S. Simon, Structural and magnetic properties of CaO-P_2O_5-SiO_2-Fe_2O_3 glass-ceramics for hyperthermia, *J. Magn. Magn. Mater*. (2005) 293, 310–313.
[10]. C. Mirestean, H. Mocuta, R.V.F. Turcu, G. Borodi, S. Simon, Nanostructurated materials for hyperthermia treatment of bone tumors, *J. Optoelectr. Adv. Mater*. (2007) 9, 764–767.
[11]. D. Predoi, M. Barsan, E. Andronescu, R.A. Vatasescu-Balcan, M. Costache, Hydroxyapatite-iron oxide bioceramic prepared using nano-size powders, *J. Optoelectr. Adv. Mater*. (2007) 9, 3609–3613.
[12]. C. Mirestean, P. Berce, S. Simon, Influence of heat treatment atmosphere on the superparamagnetic iron oxide – hydroxyapatite composites, *J. Optoelectr. Adv. Mater*. (2010) 12, 1899–1902.
[13]. S.V. Dorozhkin, Nanodimensional and nanocrystalline calcium orthophosphates, *Am. J. Biomed. Eng.* (2012) 2, 48-97.
[14]. S.I. Stupp, G.W. Ciegler, Organoapatites: materials for artificial bone. I. Synthesis and microstructure, *J. Biomed. Mater. Res*. (1992) 26, 169-183.
[15]. T.J. Webster, C. Ergun, R.H. Doremus, R.W. Siegel, R. Bizios, Enhanced osteoclast-like cell functions on nanophase ceramics, *Biomaterials* (2001) 22, 1327-1333.
[16]. J. Huang, S.M. Best, W. Bonfield, R.A. Brooks, N. Rushton, S.N. Jayasinghe, M.J. Edirisinghe, *In vitro* assessment of the biological response to nanosized hydroxyapatite, *J. Mater. Sci. Mater. Med*. (2004) 15, 441-445.

STUDIA UBB PHYSICA, Vol. 58 (LVIII), 2, 2013, pp. 83-88
(RECOMMENDED CITATION)

SOME ASPECTS ON PULSATORY CURRENT ELECTRODEPOSITION

G. MOCANU[a,*], D. POP[b]

ABSTRACT. It has been noticed that the quality parameters of electrolytic deposition are higher when an alternative current regime is used, i.e., when the voltage source controlling the electrolyte bath is pulsatory. Two temporal scales are characteristic to the source and thus to the process, the duration of the on-phase and the duration of the off-phase (also called relaxation time). A method is proposed to further improve this setting by allowing for a time-variable relaxation time. A full analytical treatment is presented, including the solution of the associated convection-diffusion equation for the ion concentration in the electrolyte bath.

Keywords: *electrodeposition, concentration, diffusion.*

INTRODUCTION

Both experimental and theoretical considerations show that, that in some cases, alternative current (AC) electrodeposition is better than direct current (DC) electrodeposition [1,2]. The classical setup in this framework consists of the AC source with constant on-and-off-phases, an electrolyte bath and two electrodes [3,4]. Although different authors suggest that the physics of the process would better be modelled by a variable off-phase [eg. 5] due to the time-changing nature of the electrolyte density etc, we are not aware of an experimental setup or a consistent theoretical discussion on this topic.

The purpose of this paper is thus to provide a first attempt at an analytical presentation of AC electrodeposition with a time-variable off-phase. In the next Section the theoretical setup is presented together with some assumptions. In Section 4 the differential equation for the ion concentration within the electrolyte bath is discussed and solved for this toy model. We consider that a parameter indicative of

[a] *Babes Bolyai University, Faculty of Physics, 1 Kogalniceanu str., 400084 Cluj Napoca, Romania*
[b] *Gheorghe Sincai Theoretical Highschool, 15A Crisan str., 450061 Zalau, Romania*
** Corresponding author: gabriela.mocanu@ubbcluj.ro*

electrodeposition quality is the current at the deposition electrode. Thus in Section 5 a comparative study is made between the current at the deposition electrode for our model and for the case of constant off-phase in an otherwise similar setting.

SETUP

What follows is a discussion on a toy model for the theoretical setting of electrodeposition and for the analytical treatment of the associated convection-diffusion equation. This discussion aims at generality and for this reason, there will be no specifications of the type of electrodes and electrolyte bath. It is obvious that particular cases can be afterwards treated in a similar manner.

There are some **assumptions** which we clearly state from the beginning

- there is no interaction between different species of ions in the electrolyte bath;
- the diffusion coefficient is constant;
- since in experimental deposition, the process which is dominant at the deposition electrode is diffusion on a length L towards the emission electrode [3], we will assume that we have an "effective" electrode responsible of emitting ions placed at a distance L with respect to the deposition electrode
- the thickening of the deposition electrode is not considered explicitly; an explicit consideration would involve changing the boundary conditions on the deposition electrode by taking a time-dependent position for this electrode.

The theoretical setup (Fig. 1) consists of the electrode on which the deposition is occurring, placed at a position $x = L$ on a Ox axis, an "effective" emission electrode, placed at $x = 0$ and an AC source controlling the process; this source is represented by some function U(t). The effective electrode has a temporal behaviour similar to that of the AC source, i.e., it releases the ions as $\sim U(t)$.

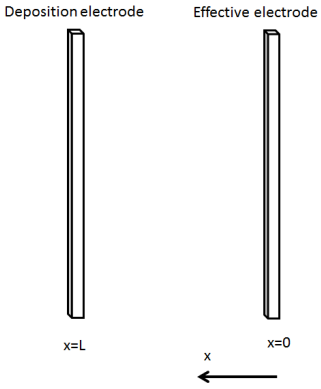

Fig. 1. Theoretical setup

We encapsulate the constant on-phase and time variable off-phase by a functional form of U(t) (Fig. 2) as

$$\boldsymbol{U(t) = \sum_{k=0}\left[H\left(t - kt_1 - \sum_{j=0}^{j=k}\tau_j\right) - H\left(t - (k+1)t_1 - \sum_{j=0}^{j=k}\tau_j\right)\right]}, \quad (1)$$

where $H(x)$ is the Heaviside Step Function, t_1 is the (constant) time period in which the source is active, $\tau = at + b$ is the (assumed) linear time dependency between the length of time the source is off and the current time,

$$\boldsymbol{\tau_j = j\, t_1 + \tau(j-1)t_1}. \quad (2)$$

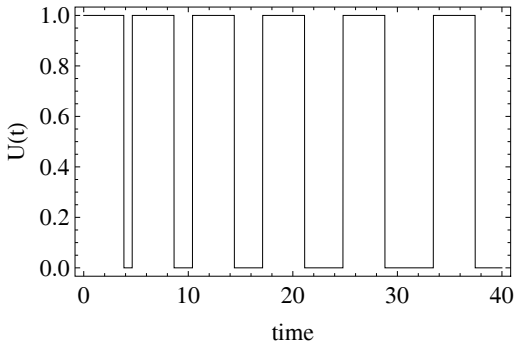

Fig. 2. Time behavior of the tension function Eq. 1,
with $t_1 = 4, a = 0.2, b = 0$ (numerical values chosen for demonstration purpose).

We will consider as a reference case the constant relaxation time case, which is a particular case of Eq. 1, with $\tau_j \equiv t_2 = const.$ (see Fig. 3)

$$\boldsymbol{U_r(t) = \sum_{k=0}\left[H\left(t - k(t_1 + t_2)\right) - H(t - k(t_1 + t_2) - t_1)\right]}. \quad (3)$$

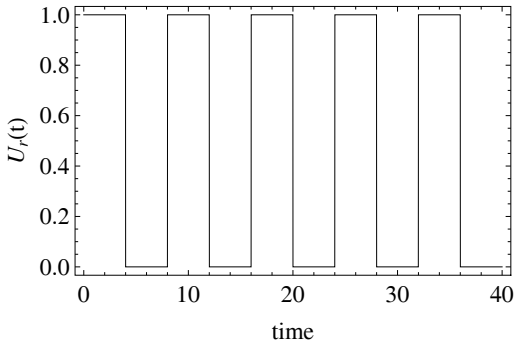

Fig. 3 Time behavior of the tension function Eq. 3,
with $t_1 = t_2 = 4$, (numerical values chosen for demonstration purpose).

SOLUTION

Let $n(x,t)$ be the ion concentration at position x and time t, with $x \in [0,L]$ and $t \geq 0$. The differential equation describing the space-time evolution of the concentration in the bath is an advective diffusion equation [6]

$$\frac{\partial n}{\partial t} = D_0 \frac{\partial^2 n}{\partial x^2} - u_0 U(t) \frac{\partial n}{\partial x}, \tag{4}$$

where

D_0 is the diffusion constant and the whole term $u_0\, U(t)$ is the time dependent convection coefficient; u_0 is a constant coefficient that connects the convection to the ion emission (which was assumed to be proportional to $U(t)$). Eq. 4 has initial condition

$$n(x,0) = 0, x \geq 0, \tag{5}$$

the first boundary condition which states that new ions are added to the effective electrode with a temporal dependency proportional to the applied tension

$$n(0,t) = N_0 U(t), t \geq 0, \tag{6}$$

where N_0 is the constant of proportionality for this process, and the boundary condition at infinity

$$\frac{\partial n}{\partial x} = 0 \; for \; x \to -\infty, t \geq 0. \tag{7}$$

This is a one dimensional linear convection-diffusion equation with time variable coefficients. An analytical solution can be obtained for this equation and a general algorithm was described in, e.g., [6].

A change in variables for $(x,t) \to (X,T)$ is performed as

$$X = \int U(t) dx = xU(t) \; which \; gives \; x = \frac{X}{U(t)} \tag{8}$$

and

$$T = \int_0^t U^2(t) dt, \tag{9}$$

when $U(t) \neq 0$.

The advection-diffusion Eq. 4 thus becomes

$$\frac{\partial n}{\partial T} = D_0 \frac{\partial n^2}{\partial X^2} - u_0 \frac{\partial n}{\partial X}, \tag{10}$$

with initial condition

$$n(X,0) = 0, X \geq 0\,, \tag{11}$$

and boundary conditions

$$n(0,T) = N_0 U(T), T > 0, \tag{12}$$

$$\lim_{X \to -\infty} \left(\frac{\partial n}{\partial X}\right) = 0, T \geq 0\,. \tag{13}$$

The advection-diffusion equation in the (X,T) domain is reduced into a diffusion equation in terms of a new independent variable, K, defined by

$$n(X,T) = K(X,T) exp\left\{\frac{u_0 X}{2D_0} - \frac{u_0^2 T}{4D_0}\right\}. \tag{14}$$

Then Eq. 10 becomes

$$\frac{\partial K}{\partial T} = D_0 \frac{\partial^2 K}{\partial X^2}, \tag{15}$$

which has the familiar form a diffusion equation for $K(X,T)$ with constant diffusion coefficient; the initial and boundary conditions for the new variable-function $K(X,T)$ are

$$K(X,0) = 0, X \geq 0, \tag{16}$$

$$K(0,T) = N_0 U(T) exp\left\{\frac{u_0^2 T}{4D_0}\right\}, T > 0, \tag{17}$$

$$\frac{\partial K}{\partial X} + K \frac{u_0}{2D_0} = 0 \; as \; X \to -\infty, T \geq 0. \tag{18}$$

Obtaining a solution for this equation is in many ways "classical". First, use a Laplace transform to discard the time derivative

$$\bar{K}(X,p) = \int_0^\infty K(X,T) e^{-pT} dT \tag{19}$$

and obtain

$$p\bar{K} = D_0 \frac{\partial^2 \bar{K}}{\partial X^2}. \tag{20}$$

Rearrange this as

$$\frac{\partial^2 \bar{K}}{\partial X^2} - \frac{p}{D_0} \bar{K} = 0, \tag{21}$$

with

$$\bar{K}(0,p) = N_0 \int_0^\infty U(T) exp\left\{\frac{u_0^2 T}{4D_0}\right\} exp\{-pT\} dT, \tag{22}$$

and

$$\frac{\partial \bar{K}}{\partial X} + \frac{u_0}{2D_0} \bar{K} = 0 \; as \; X \to -\infty. \tag{23}$$

The solution which satisfies the boundary conditions is

$$\bar{K}(X,p) = \bar{K}(0,p) exp\left\{\sqrt{\frac{p}{D_0}} X\right\}. \tag{24}$$

The solution to our problem (in variables (X,T)) is

$$n(X,T) = L^{-1}\{\bar{K}(X,p)\} exp\left\{\frac{u_0 X}{2D_0} - \frac{u_0^2 T}{4D_0}\right\}, \tag{25}$$

where $f(T) = L^{-1}\{\bar{f}(p)\}$ is the inverse Laplace transform of $\bar{f}$(p).

One of the ways to assess the quality of a deposition is by calculating the current of ions at the deposition electrode for a certain elapsed time.

The current of ions at the deposition electrode and after a number *j* of periods of the applied electrical tension, i.e. for $t = jt_1$ (this in turn fixes *T* to T_j through Eq. 9) is

$$I(X_L, T_j) \propto n(X_L, T_j). \tag{26}$$

Thus a comparison of the quality of the deposition with respect to the reference case can be made by taking the ratio between the current at the electrode in our model with respect to the current at the electrode for the reference case

$$\xi = \frac{n(X_L, T_j)}{n_r(X_L, T_r)}. \tag{27}$$

Care should be taken when calculating both X_L and T_j, as they depend on the specific shape of the $U(t)$ used (through equations 8 and 9 respectively). This ξ depends on a large number of parameters (i.e., a, b, u_0, t_1, t_2 etc.), and the relative importance of them will be discussed in a future paper, complementary to experimental data.

CONCLUSIONS

In the context of an AC electrodeposition regime, an analytical method has been discussed which allows considering a time-variable off-phase for the voltage source controlling the electrolyte bath. The ion concentration in the electrolyte bath and thus the quality of deposition can be computed when the specific time dependency of the AC voltage source is known.

REFERENCES

[1]. P.M. Viaceslavov, "Depunerea electrolitica a aliajelor", Editura tehnica, Bucuresti, 1974, chapter 7.
[2]. H. Karami, H. Babaei, *Int. J. Electrochem. Sci*, 7, 601-614 (2012).
[3]. M. Teodorescu, L. Vladescu, "Tehnica masurarii marimilor fizico-chimice si aparatura de laborator", Editura Tehnica si Pedagogica, Bucuresti, 1994.
[4]. Lou, H.H. and Y.L. Huang, "Electroplating", *Encyclopedia of Chemical Processing*, S. Lee (ed.), Marcel Dekker, New York, NY, 2006.
[5]. M.S. Chandrasekar, M. Pushpavanam, *Electrochimica Acta*, 53, 3313-3322 (2008).
[6]. D.K. Jaiswal, A. Kumar, R.R. Yadav, *Analytical solution to one-dimensional advection-diffusion equation temporally dependent coefficients,* J. of Water Resource and Protection, 3, 76-84 (2011).